DIFFUSION TENSOR IMAGING: EVALUATION OF TRACTOGRAPHY ALGORITHM PERFORMANCE USING GROUND TRUTH PHANTOMS

By

Alexander J. Taylor

A Thesis Submitted to the Graduate Faculty of the Virginia Polytechnic Institute and State University in Partial Fulfillment of the Requirements for the Degree of

Master of Science
in
Electrical Engineering

Chistopher L. Wyatt, Ph.D., Chair

A. Lynn Abbott, Ph.D.
Puskin Kachroo, Ph.D.

May, 2004
Blacksburg, Virginia

Keywords: Diffusion Tensor Imaging, Magnetic Resonance Imaging, Tractography, Fast Marching Method, Streamline, Phantom

DIFFUSION TENSOR IMAGING: EVALUATION OF TRACTOGRAPHY ALGORITHM PERFORMANCE USING GROUND TRUTH PHANTOMS

Alexander J. Taylor

(Abstract)

Diffusion Tensor Magnetic Resonance Imaging (DT-MRI), also known as Diffusion Tensor Imaging (DTI), is a unique medical imaging modality that provides non-invasive estimates of White Matter (WM) connectivity based on local principal directions of anisotropic water diffusion. DTI tractography estimates are a macroscopically sampled description of underlying microscopic structure, and are therefore of limited validity. The under-sampling of underlying white matter structure in DTI data gives rise to Intra-Voxel Orientational Heterogeneity (IVOH), a condition in which white matter structures of multiple different orientations are averaged into a single DTI voxel sample, causing a loss of validity in the diffusion tensor model. Fast Marching Tractography (FMT) algorithms based on fast marching level set methods have been proposed to better handle the presence of IVOH in DTI data when compared to older Streamline Tractography (SLT) methods. However, the actual performance advantage of any tractography algorithm over another cannot be conclusively stated until a ground truth standard of comparison is developed.

This work develops an optimized version of the FMT algorithm that is dubbed the Front Propagation Tractography (FPT) algorithm. The FPT algorithm includes unique approaches to the speed function, connectivity estimation, and likelihood estimation components of the FMT framework. The performance of the FPT algorithm is compared against the SLT algorithm using ground truth software phantom data and human brain data. Software phantom ground truth experiments compare the performance of each algorithm in single tract and crossing tract structures for vary-

ing levels of diffusion tensor field perturbation. Human brain estimates in the corpus callosum yield qualitative comparisons from inspection of 3D visualizations. A final area of exploration is the construction and analysis of a ground truth physical DTI phantom manifesting IVOH.

Acknowledgements

First, I would like to thank Dr. Chris Wyatt for his guidance, advice, and direction throughout the course of my research. Dr. Wyatt's technical ability and down to earth kindness was vital to the completion of this project. I realize that very few professors would have allowed me such freedom in choosing the course of my research, and for that freedom I am thankful.

My next big thank you is to the Via family and the Bradley Department of Electrical and Computer Engineering for awarding me with the Bradley Fellowship during my graduate studies. I greatly appreciate being given the opportunity to complete my research distracted by work or financial worries. I hope that the Bradley Fellowship will continue far into the future and allow other fortunate students to pursue their own research visions.

I would like to express my appreciation to some important people that made this project possible. Thanks to Dr. Kraft at the Wake Forest University Baptist Medical Center for devoting your weekend and evening hours to scanning my phantoms. You proposed several good ideas, and we kept at it, I am sure we would have come up with a completely operational phantom. Thanks to Dr. Abbott and Dr. Kachroo for serving as my committee members and providing helpful feedback on my project.

I would also like to express gratitude to my family for your support during this phase of my life. You may not have always understood exactly what my problems were, but you were always a comfort and helped me to keep things in perspective. A special thanks to my sister Sydney for helping me to see the world through younger eyes.

On a more personal note, I would like to thank my good friend Daniel Hibbard for his support over the past six years. I am lucky to have such an influential and talented friend.

Allow me to thank some inanimate objects, musicians, and foods/beverages that were of aid to me during the course of things. Thanks to my IPOD for being an oasis of sanity during some long lonely nights in the lab. The following three musical artisans remind me of this project, and will therefore be documented for posterity: Out Hud, Manitoba, and Explosions in the Sky. Coffee, I couldn't have done it without you. Take-out-sushi, thanks for the much needed nutrition.

Finally, I would like to thank some friends (in no particular order) that offered spirited conversation, advice, companionship, and shelter during these past two years. Special thanks to: Dr. Besieris, Kyong Soh, Jeremy Barry, Aaron Orndorff, Craig and Emily Berman, Steve Pond, Kimmy Reese, Scott Pellet, and Xanja Von Barry.

Table of Contents

List of Figures

List of Abbreviations

ADC	Apparent Diffusion Coefficient
DTI	Diffusion Tensor Imaging
DWI	Diffusion Weighted Imaging
EPI	Echo-Planar Imaging
FPT	Fast Propagation Tractography
HARD	High Angular Resolution Diffusion
IVOH	Intravoxel Orientational Heterogeneity
MRI	Magnetic Resonance Imaging
ODF	Orientation Density Function
PEV	Principal Eigenvector
PDE	Partial Differential Equation
PDF	Probability Density Function
PV	Partial Volume
SLT	Streamline Tractography
SNR	Signal to Noise Ratio
WM	White Matter

Chapter 1

Introduction and Background

1.1 Introduction

Diffusion Tensor Magnetic Resonance Imaging (DT-MRI), also known as Diffusion Tensor Imaging (DTI), has shown promise as a non-invasive tool for estimating the orientation and quantity of White Matter (WM) tracts in vivo. The process of using DTI data to estimate white matter structures is commonly known as tractography. DTI tractography is a unique imaging modality in that it offers the only clinically applicable means of non-invasively imaging the myelinated axonal structure of the human brain.

The ability of DTI to quantitatively describe white matter connectivity in the human brain has a variety of clinical applications. The correlation between white matter structural asymmetries and schizophrenia is currently being investigated in group studies [23]. Similar group studies are being conducted to gain an understanding of the progression of white matter tract damage in neuro-degenerative diseases such as Alzheimer's disease [31]. Changes in the diffusion directional dependence, known as diffusion anisotropy, have been illustrated to have promise in detecting and characterizing brain tumors [40]. DTI has been used to characterize reductions in diffusion anisotropy in regions of severe brain trauma trauma that are theorized to result from from tissue swelling [17]. It is hoped that DTI will provide insights into the progression of tissue damage in cases of severe injury, and that these insights could provide strategies to limit the spread of tissue damage [17].

Current hardware limitations in MRI scanners limit the minimum spatial voxel resolution in DTI data to the order of a millimeter. DTI tractography is therefore

1

a macroscopic model of a microscopic structure and is prone to erroneous estimates when tracts of two or more distinct orientations are present in the same voxel. This condition of having two or more fiber bundles of different directions in the same voxel is known as Intra-Voxel Orientational Heterogeneity (IVOH) [35]. The existence fiber crossings and branches in human neural anatomy creates an issue as to the range of applicability of DTI tractography estimates based on macroscopically sampled data. Given the scale of DTI data, it is reasonable to apply tractography estimation to clinical applications that call for a gross estimation of connection densities in two different regions of the brain, as is done in clinical group studies. The accuracy of white matter anatomical maps obtained by DTI is more unclear due to the general inability of the diffusion tensor model to describe multiple orientational maxima within a single voxel.

The central objective of this thesis is to investigate how tractography algorithms react to the presence of tract crossings and noise perturbations in DTI data. Toward this goal, the performance of two different tractography algorithms are compared. A streamline algorithm is implemented based on the algorithmic framework developed by Basser et al. [2]. The streamline method represents a baseline in the progression of DTI algorithms, allowing for a reference of comparison to modern front propagation techniques. A front propagation algorithm dubbed the Front Propagation Tractography (FPT) algorithm is developed based on the Front Marching Tractography (FMT) algorithm proposed by [27]. Significant contributions are proposed in the FPT algorithm including the definition of a speed function based on an Orientation Density Function (ODF), a discrete greedy search method of connectivity estimation, and a new definition for a tract likelihood estimate.

Two different types of ground truth DTI data are investigated in this research for cases of IVOH. A unique methodology of creating simulated linear tensor field crossing phantoms is proposed. The software phantom crossing takes into account current evidence as to the planar geometry and orientational ambiguity of diffusion

tensor fields in regions of IVOH [35]. A non-biological physical ground truth phantom containing tract crossings is also attempted. Published physical phantom results have been limited to this point to single tract biological tissue studies [13].

The study of noise effects on tractography estimates is undertaken from the level of the diffusion tensor. Perturbations are added to diffusion tensor elements for purposes of simulating the impact of noise in diffusion weighted measurements on diffusion tensor fields. The effect of noise perturbations on single tract software simulations of linear and helical geometry is investigated. A comprehensive simulation of tractography algorithm performance for tract crossings of various intersection angles and diffusion tensor perturbation levels is also conducted in which no *a-priori* knowledge is assumed as to the curvature of underlying white matter structure.

This thesis is organized as follows. First, chapter one discusses necessary background and pertinent literature related to diffusion tensor imaging. Next, chapter two provides a discussion of experimental methods. Two different tractography algorithms are developed in chapter two: a standard streamline approach, and a modification of the Fast Marching Tractography (FMT) algorithm proposed in [27] that will be referred to as the Front Propagation Tractography (FPT) algorithm. Chapter two also describes the implementation of software and physical DTI ground truth phantoms. Finally, chapter three presents a detailed comparison of the SLT and FPT tractography algorithms. Quantitative comparisons of performance in both algorithms are made using results from software phantom ground truth experiments. Qualitative comparisons are made using human brain data in the corpus callosum region of the brain. The final portion of chapter three provides a conclusion and a discussion of future work.

1.2 Theoretical background

1.2.1 Diffusion physics

Diffusion is a microscopic phenomenon arising from thermal motion in which molecules migrate randomly. Molecular diffusion motion is also referred to as Brownian motion. Einstein's relation develops a time distance relationship for a particle undergoing Brownian motion in free space [34],

$$D = \frac{1}{6\tau} r^2 \,, \tag{1.1}$$

where D is a scalar known as the diffusion coefficient, τ is the period of time during which a particle undergoes Brownian motion, and r is net displacement. The diffusion coefficient D relates time to the square displacement, and is therefore not a diffusion velocity [5].

In the case of a restrictively bounded environment, particles undergoing Brownian motion are displaced with greater magnitudes in directions parallel to boundaries, and smaller magnitudes in directions which oppose boundaries [34]. Thus, directionally dependent Brownian motion reflects the underlying structure of a bounded environment [34]. Diffusion is said to be anisotropic when displacement due to Brownian motion is directionally dependent. In cases of anisotropic diffusion, Einstein's relation must be generalized to allow for directional dependence [34],

$$\mathbf{D} = \frac{1}{6\tau} < \hat{\mathbf{r}}\hat{\mathbf{r}}^{\mathbf{t}} > \,, \tag{1.2}$$

where $\mathbf{D}$ is a second order tensor, and $\hat{\mathbf{r}}$ is a displacement vector indicating both the magnitude and direction of Brownian motion. The tensor $\mathbf{D}$ in the generalized form of Einstein's relation is known as a diffusion tensor.

In general, the diffusion tensor $\mathbf{D}$ depends on particle mass, the structure of the medium, and temperature [5]. In DTI, the particle mass of water molecules and the temperature at which measurements are conducted is assumed constant. This

assumption allows for the spatial fluctuation of the diffusion tensor in DTI to be interpreted solely in terms of local anatomical structure.

The process of diffusion may also be viewed at a macroscopic level in terms of a group of moving particles. Fick's first equation describes the effect of diffusion on the motion of nonuniform distributions of particles [5],

$$\hat{\mathbf{J}} = -D\nabla C(\mathbf{r}) \, , \tag{1.3}$$

where $\hat{\mathbf{J}}$ is a vector representing the magnitude and direction of particle flux, D is the coefficient of diffusion in the $\hat{J}$ direction, and $C(\mathbf{r})$ is a scalar valued function that describes the concentration of particles at a given position $\mathbf{r}$. Fick's first equation states that the flux of particles in a system is proportional to the gradient of the particle concentration. Therefore, Equation 1.3 predicts an equilibrium of zero particle flux for systems with an even spatial distribution of particles where $C(\mathbf{r})$ is constant. The negative constant of proportionality next to the gradient of $C(\mathbf{r})$ on the right hand side of Equation 1.3 is the basis for the understanding of diffusion as the tendency of particles in a system to move from areas of greater concentration to areas of lesser concentration.

1.2.2 The anatomy of neural white matter and diffusion tensor imaging

Neurons are the physical structures in the nervous system that transmit information in the form of nerve impulses from one part of the body to another. Neurons are composed of three basic parts: the cell body, the axon, and dendrites [33]. Dendrites are attached to the neuron cell body, and receive impulses from other neurons at synapses [33]. Axons are long cable-like structures that transmit impulses away from dendrites and the cell body. Axons are wrapped by a thin layer of connective tissue known as the endoneurium [16]. Groups of wrapped axons are bundled together into tracts, or fascicles, by a thin boundary known as the perineurium [16].
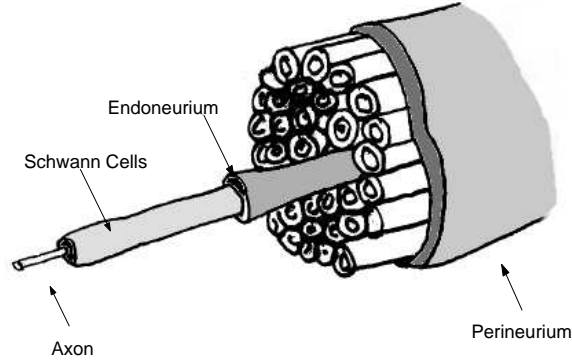
Figure 1.1: Illustration of myelinated fiber tract

The portion of the fascicles in the human brain that contain white fatty myelinated Schwann cells form the white matter of the brain [33]. The mobility of water to diffuse across tracts with myelinated boundaries is restricted, causing water to diffuse anisotropically in greater amounts in directions parallel to fiber tracts and lesser amounts of diffusion in directions to boundaries [38] [10] [11]. This physical situation of increased water diffusion in directions parallel to myelinated fascicles is what is measured by diffusion weighted imaging to construct diffusion tensors and resulting tractography estimates.

1.2.3   Diffusion weighted imaging and the diffusion tensor

Diffusion weighted images use diffusion gradient pulses to estimate a relative amount of water diffusion in a measurement direction $\hat{g}$ (Figure 1.2). Diffusion weighted images are the raw data source used to calculate the diffusion tensor. Diffusion weighted images are measured using the Stejskal-Tanner imaging sequence. A Stejskal-Tanner imaging sequence may be implemented by adding diffusion gradient pulses to standard anatomical MRI pulse sequences. In the most simple example, a Stejskal-Tanner pulse sequence may implemented using a spin-echo MRI imaging sequence with the
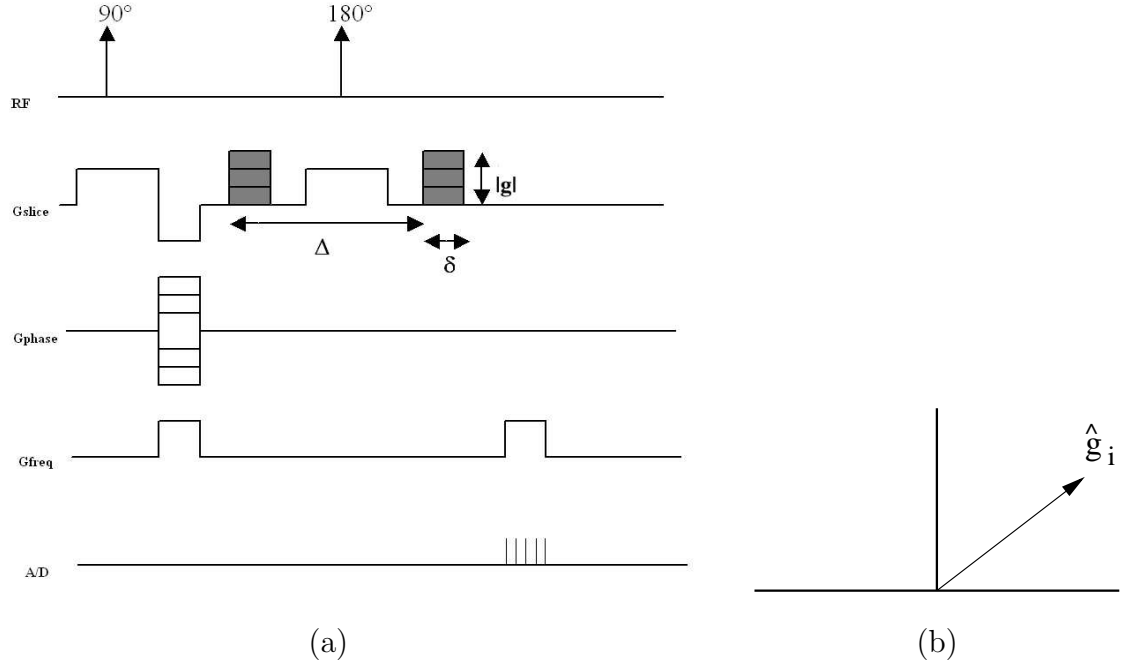
Figure 1.2: (a) Spin-echo Stejskal-Tanner imaging pulse sequence (b) Illustration of directional sampling of diffusion gradient pulse in direction $\hat{g}_i$.

addition of two diffusion-encoding gradients [38]. Figure 1.2 (a) is an illustration of a spin-echo Stejskal-Tanner pulse sequence.

The addition of two gradient pulses **g** symmetrically positioned about the 180 degree phase correction RF pulse allows for measurement of spin drift in a given direction $\hat{g}$. Spins not undergoing motion in the $\hat{g}$ direction are refocused completely by application of the 180 degree phase refocusing pulse followed by a repetition of the gradient pulse **g**. Spins undergoing Brownian motion during the time between gradient pulses, τ_d, do not phase refocus completely following the application of the second gradient pulse, resulting in signal loss.

In practice, diffusion-weighted images are often acquired using faster Echo-Planar Imaging (EPI) sequences to reduce acquisition time [20]. EPI sequences are the fastest type of MRI imaging sequence [36]. EPI sequences obtain the complete set of planar k-space measurements used to construct a planar DWI image using only one

RF excitation, compared to the several RF/phase selection repetitions required to traverse k-space using a spin-echo sequence. Although EPI sequences offer improved acquisition times and reduce motion artifacts, EPI sequences are subject to distortions due to the eddy currents introduced by the large diffusion gradients used in DWI measurements. A body of research has focused on eddy-current distortion correction in DWI images. As an example, work by [20] has proposed a mutual information based registration method to correct eddy current distortions by registering each planar DWI image with a non-diffusion weighted T-2 image. The preprocessing-processing tools and tractography algorithms developed for use in this work assume that some manner of eddy-current correction has been implemented on DWI measurements prior to computation of the diffusion tensor.

The relationship between loss of phase coherence in the transverse spin RF signal and the gradient pulse **g** is given by the Stejskal-Tanner equation [38],

$$S_i = S_0 e^{-b \hat{\mathbf{g_i}}^T \mathbf{D} \hat{\mathbf{g_i}}} \ , \tag{1.4}$$

where b is the diffusion weighting factor [38] given by

$$b = \gamma^2 \delta^2 [\Delta - (\delta/3)] |\mathbf{g}|^2 \ . \tag{1.5}$$

In Equation 1.5, γ is the Lamor constant, δ is the gradient pulse width, Δ is the time between gradient pulses, $|\mathbf{g}|$ is the strength of the diffusion gradient pulses, S_0 is the RF signal received for a measurement without diffusion gradient pulses, and S is the signal received with diffusion gradient pulses.

Using the three-dimensional Gaussian Stejskal-Tanner model, the six unique elements of the diffusion tensor **D** may be solved by acquiring at least six diffusion weighted measurements in non-collinear measurement directions $\hat{g}_i$ along with a non-diffusion-weighted measurement S_0. Taking more than six diffusion weighted measurements creates an over constrained system of equations which may be solved using least square methods or the use of M-estimators [20] [21]. The advantage of over-constraining the solution for **D** is a reduction in the amount of noise propagating

from diffusion weighted measurements S_i into the calculated diffusion tensor. The linear system of $n \geq 6$ diffusion weighted measurements constraining the diffusion tensor D may be represented in matrix form [21].

$$
\begin{bmatrix}
x_1^2 & y_1^2 & z_1^2 & 2x_1y_1 & 2y_1z_1 & 2x_1z_1 \\
x_2^2 & y_2^2 & z_2^2 & 2x_2y_2 & 2y_2z_2 & 2x_2z_2 \\
x_n^2 & y_n^2 & z_n^2 & 2x_ny_n & 2y_nz_n & 2x_nz_n
\end{bmatrix}
\begin{bmatrix}
Dxx \\
Dyy \\
Dzz \\
Dxy \\
Dyz \\
Dxz
\end{bmatrix}
=
\begin{bmatrix}
\frac{-1}{b}ln\frac{S_1}{S_0} \\
\frac{-1}{b}ln\frac{S_2}{S_0} \\
\frac{-1}{b}ln\frac{S_n}{S_0}
\end{bmatrix}
\tag{1.6}
$$

In the linear system of equations $\mathbf{Ad = s}$ of Equation 1.6, $\mathbf{A}$ is the encoding matrix containing the $n \geq 6$ unit normalized gradient measurement directions, $\mathbf{d}$ is a vector specifying the 6 unique elements of the diffusion tensor $\mathbf{D}$, and $\mathbf{s}$ is a vector containing natural logarithmic scaled RF signal loss resulting from the Brownian motion of spins.

A least squares approach was used to solve Equation 1.6 for $\mathbf{D}$. Least squares problems may be solved by using the pseudo-inverse $\mathbf{A}^{\dagger}$ via the Singular Value Decomposition (SVD) of $\mathbf{A}$ [18]

$$
\mathbf{A}^{\dagger} = <\mathbf{VS^{-1}U^{T}}> , \tag{1.7}
$$

where $\mathbf{U}$ and $\mathbf{V}$ are orthogonal matrices, and $\mathbf{S}$ is a diagonalized matrix containing the singular values of $\mathbf{A}$. The least squares estimate for the diffusion tensor $\mathbf{D}$ is given by

$$
\mathbf{d} \cong <\mathbf{A}^{\dagger}\mathbf{s}> . \tag{1.8}
$$

1.2.4 Tensor analysis and the diffusion tensor

A tensor of order n is a mathematical construct whose specification in any given three dimensional coordinate system requires 3^n numbers, called the components of the tensor [7]. Therefore, a scalar is a tensor of order zero and a vector is a tensor of order one. The term tensor is used to describe what is more specifically a second order tensor. For the sake of brevity, this convention of using the term tensor to refer to a second order tensor will be adopted when referring to the second order diffusion tensor $\mathbf{D}$.

A second order tensor may be represented as a 3 x 3 matrix.

$$\mathbf{B} = \begin{bmatrix} B_{11} & B_{12} & B_{13} \\ B_{21} & B_{22} & B_{23} \\ B_{31} & B_{32} & B_{33} \end{bmatrix} \tag{1.9}$$

Using this matrix form, a tensor may be interpreted as a function $f(\hat{\mathbf{a}})$, $f : R^3 \rightarrow R^3$, that maps an input vector $\hat{\mathbf{a}}$ to an output vector of different orientation and magnitude [7].

$$f(\hat{\mathbf{a}}) = < \hat{\mathbf{a}}\mathbf{B} > \tag{1.10}$$

The Diffusion Tensor $\mathbf{D}$ is a real, symmetric second order tensor, represented in matrix form as a real, symmetric 3x3 matrix.

$$\mathbf{D} = \begin{bmatrix} D_{11} & D_{12} & D_{13} \\ D_{12} & D_{22} & D_{23} \\ D_{13} & D_{23} & D_{33} \end{bmatrix} \tag{1.11}$$

Diagonalization of the diffusion tensor results in a set of three eigenvectors $\hat{v}_1, \hat{v}_2, \hat{v}_3$ with associated eigenvalues $\lambda_1, \lambda_2, \lambda_3$ listed in decreasing order. The eigensystem of the diffusion tensor may be interpreted graphically as an ellipsoidal surface with semi-major axis oriented in the $\hat{v}_1$ direction and semi-minor axis oriented in the $\hat{v}_2$ and $\hat{v}_3$

(a)   (b)
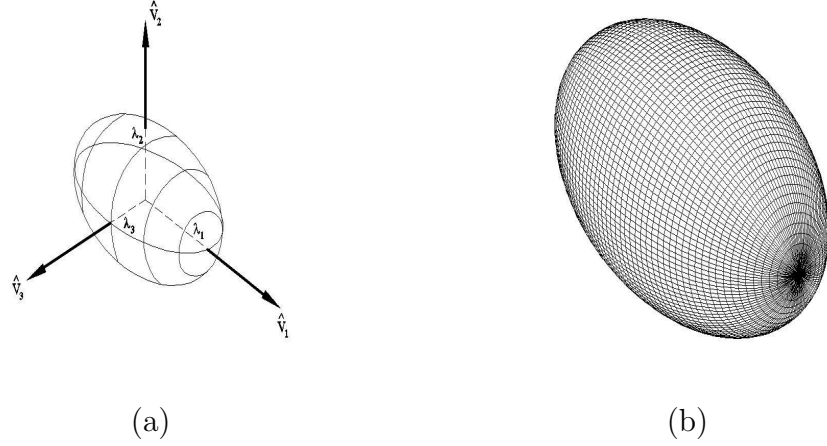
Figure 1.3: Graphical interpretation of a symmetric tensor in terms of an ellipsoid. (a) Eigensystem of symmetric tensor as relates to ellipsoid orientation and axis lengths. (b) Wire mesh view of ellipsoid.

directions. The lengths of the axis in this ellipsoidal interpretation are given by the corresponding eigenvalues of each eigenvector, with semi-major axis length λ_1 and semi-minor axis lengths λ_2 and λ_3. In order for the analogy between the symmetric real tensor and the ellipsoid to be physically realizable, the eigenvalues of $\mathbf{D}$ must be non-negative. The analogy between the diffusion tensor and an ellipsoidal surface is most intuitive when viewed graphically as in Figure 1.3.

The axis lengths of the diffusion ellipsoid defined by the eigenvalues of the diffusion tensor represent magnitudes of diffusion at a global position $r = (x, y, z)$ in the local coordinate system $\hat{v}_1, \hat{v}_2, \hat{v}_3$. Because the eigenvectors of the diffusion tensor are composed of global $\hat{x}, \hat{y}, \hat{z}$ components, the eigensystem of the diffusion tensor represented by the diffusion ellipsoid provides orientation invariant estimates of diffusion in the global orthonormal coordinate system [9]. In cases of purely isotropic diffusion, the diffusion ellipsoid takes on a spherical shape, as $\lambda_1 = \lambda_2 = \lambda_3$. There are two extreme cases of physically realizable anisotropic diffusion in which the ellipsoidal description of Figure 1.3 degenerates. For purely linear anisotropic diffusion, $\lambda_1 = c$

and $\lambda_2 = \lambda_3 = 0$, the diffusion ellipsoid degenerates into a line pointing in the v_1 direction. In the case of purely planar anisotropic diffusion, the diffusion ellipsoid becomes oblate, meaning that $\lambda_1 = \lambda_2, \lambda_3 = 0$

The degree of anisotropy in the diffusion tensor is commonly represented by the Fractional Anisotropy (FA) scalar metric.

$$FA = \frac{\sqrt{(\lambda_1 - \lambda_2)^2 + (\lambda_2 - \lambda_3)^2 + (\lambda_1 - \lambda_3)^2}}{\sqrt{2(\lambda_1^2 + \lambda_2^2 + \lambda_3^2)}} \tag{1.12}$$

For physically realizable diffusion tensors with non-negative eigenvalues, the FA of a diffusion tensor is normalized between zero and one. In an extreme case, a FA value of one denotes a diffusion tensor in which $\lambda_1 = c$ and $\lambda_2 = \lambda_3 = 0$ and diffusion is completely anisotropic in the direction of v_1. The fractional anisotropy metric evaluates to zero in the opposite extreme of a completely isotropic diffusion tensor. In general, higher values of FA occur for diffusion tensors in which local diffusion has a higher degree of anisotropy.

It should be noted that a relatively small amount of non-physically realizable, non-positive-semi-definite diffusion tensors $\mathbf{D}$ arise in computed diffusion tensor fields due the effect of outlying DWI measurements on regression estimates of $\mathbf{D}$ [20]. In non-physical regression estimates for $\mathbf{D}$, both the ellipsoidal geometry assumed in the diffusion tensor model and the zero to one normalization assumed in the FA metric no longer hold. Although not commonly mentioned in DTI literature, the existence of non-physically realizable diffusion tensors must sometimes be accounted for as a special case in tractography algorithms.

1.3 Literature review of DTI tractography

Diffusion tensor imaging is limited in its ability to accurately describe local tract orientation in cases of branching or crossing structure. Because the ellipsoidal geometry associated with the Gaussian tensor model has only one orientational maximum, the

tensor model is inadequate when multiple tract orientations exist within a single voxel [27]. This limiting case of DTI tractography in which multiple distinct fiber orientations are captured within a single voxel sample is known as Intra-Voxel Orientational Heterogeneity (IVOH) [35]. In cases of IVOH, the best a tractography algorithm using a single Gaussian diffusion tensor model can hope to accomplish is to accurately estimate crossing or branching tracts up to a point of intersection, and then infer the existence of the intersection.

Current DTI tractography research focuses on the use of multi-tensor mixture models [35] and higher order tensor models [25] that allow for multiple orientational maxima of diffusion. The multi-tensor model proposed in [35] additively mixes Gaussian diffusion tensors until a set of N tensors is found that best explains observed diffusion weighted measurements. In practice, it was shown that the multi-tensor mixture method yields stable results for up to N=2 tensors, allowing for the detection of up to two tract orientations within a single voxel. An 8th order generalized diffusion tensor model was demonstrated in [25] to accurately describe diffusion displacement probabilities for tract crossings of up to three distinct orientations. The angular resolution required for the construction of more advanced diffusion tensor models increases with model complexity. For a generalized diffusion tensor model of order L, a minimum of $N \geq (L + 1)(L + 2)/2$ DWI measurements must be obtained [25]. In the case of a bi-exponential model, a minimum of $N \geq 13$ DWI measurements are required for a constrained solution. The improved orientational information provided by higher angular resolution models is only meaningful if spatial resolution is also increased to reduce voxel sizes to a scale closer to the μm scale of WM tracts. In [25], diffusion weighted measurements used to construct 8th order tensors were sampled at $150\mu m$ x $150\mu m$ x $300\mu m$, which is significantly higher spatial resolution than the mm scale resolution available on low to mid field clinical 1.5-3 T MRI scanners. The focus of this research was restricted to the use of standard clinical MRI equipment and therefore the greater complexity associated with more advanced diffusion

tensor models was not worthwhile. The remainder of the document will focus entirely on single Gaussian diffusion tensor tractography.

Current research indicates that cases of crossing and diverging white matter do in fact occur, making IVOH a legitimate hurdle in DTI tractography. On a macroscopic scale, tract divergence can be noted in relatively large neural structures such as the corona radiata [27]. It is reasonable to assume that crossing and diverging tract structure continues to occur at and below the resolution at which DTI data is collected. It is theorized that IVOH in DTI data gives rise to oblate (planar) diffusion tensors, and the presence of regions of planar tensors has been noted in human DTI data, suggesting that IVOH occurs at a microscopic scale [35].

Hardware constraints currently limit spatial resolution of DWI measurements to the macroscopic mm level. Neural tract structures vary in diameter in different regions of the brain with diameters ranging on the scale of 1-50 μm. DTI tractography results within a voxel are therefore a macroscopic estimate of underlying microscopic structure, making the probability of IVOH reasonably high. In the event tracts do not cross within a single voxel sample, DTI tractography results are still subject to partial volume effects. Take for example the case where a group of tracts splays within a single sample. In this case, it is likely that DTI tractography describes the average orientation of the splaying tracts along the axis of symmetry. Unless tracts are bundled within large groups of homogeneous orientation, the validity of DTI anatomical maps is questionable due to the effects of partial voluming and IVOH.

The presence of noise during DWI measurements causes perturbations in the geometry and orientation of resulting diffusion tensors [1]. Noise perturbations in $\mathbf{D}$ cause directional dispersion in tract estimates [19]. The angular resolution over which diffusion weighted measurements are taken affects the upper limit of noise propagation in DTI data. The upper limit of noise propagation in computed diffusion tensors is given by the condition number of the encoding matrix, $\kappa(\mathbf{A})$ [4],

$$\kappa(\mathbf{A}) = ||\mathbf{A}||||\mathbf{A}^{-1}|| \geq \frac{Error_{D_{rel}}}{Error_{s_{rel}}} , \qquad (1.13)$$

where $\mathbf{A}$ is the encoding matrix of Equation 1.6 and $\frac{Error_{\mathbf{D}_{rel}}}{Error_{\mathbf{s}_{rel}}}$ is a ratio of error in the constructed diffusion tensor $\mathbf{D}$ relative to the error in diffusion weighted measurements $\mathbf{s}$. The noise propagation upper bound described by the condition number of the encoding matrix is impacted by both the number of directions in which a ADC data is acquired and the choice of sampling directions. The lower limit of the condition number is bounded by $\kappa(A) \approx 1.5811$ in the limit where the number of DWI measurements tends to infinity [4]. For isotropic angular resolution, the condition number monotonically decreases as the number of diffusion weighted measurements constraining the diffusion tensor increases.

A large area of tractography research is regularization of the diffusion tensor field. Regularization methods attempt to smooth the diffusion tensor field without removing orientational or anisotropy information corresponding to tract structures. In [28], an anatomical assumption is made that there is *a-priori* knowledge of low curvature within a local neighborhood of the principal eigenvector. This leads to the application of Markov random field theory to curvature limit the principal eigenvector field $\mathbf{V}$ via the minimization of an energy function E($\mathbf{V}$). Continuous partial differential equation based techniques have also been applied to regularize the diffusion tensor field in terms of an energy minimization/curvature minimization concept [12], promising faster processing capabilities when compared to [28]. The scalar concept of deformable registration has also been applied to the regularization of diffusion tensor fields [39]. In [39], volume neighborhoods are iteratively defined and repositioned according to a spatial transformation and the orientation and geometry within neighborhoods of diffusion tensors remains constant.

In this work, the diffusion tensor field $\mathbf{D}$ is not regularized previous to performing tractography estimates. Because diffusion tensor regularization methods place *a-priori* constraints on the diffusion tensor field during re-alignment of the field, crossing tracts may be unfairly removed by regularization due to high local curvature in underlying WM structure. Because a goal of this research was to compare algorithm

performance in the presence ground truth structures manifesting IVOH, no *a-priori* knowledge of local tract curvature is assumed prior to tract estimation. Although no analysis of IVOH effects are preformed during estimation of the corpus callosum in the human brain, it will be shown that the homogeneous nature of the diffusion tensor field in the corpus callosum allows for tract estimation without regularization.

Streamline Tractography (SLT) is the original method of DTI tract estimation and has become a reference of comparison for newer tractography algorithms. As such, the following paragraph will focus entirely on the basic Euler's method SLT algorithm [2] [3] [11]. Streamline tractography uses the orientational maximum of the diffusion tensor described by the eigenvector $\hat{v}_1$ with the largest corresponding eigenvalue λ_1, also known as the Principal Eigenvector (PEV), as an estimate of local tract orientation. In regions of large tract bundles on the order of voxel size or larger with homogeneous orientation, it has been verified that the principal eigenvector of the diffusion tensor accurately approximates local tract direction [19] [37]. SLT uses the principal eigenvector orientation to compute a Euler's method approximation to the parameterized tract $\mathbf{r}(s)$.

$$\mathbf{r}(s_1) = \mathbf{r}(s_0) + \alpha\hat{t}(s) \approx \mathbf{r}(s_0) + \alpha\hat{v}_1(s) \tag{1.14}$$

In Equation 1.14, tracts are computed using piecewise linear steps of size α in the direction of the principal eigenvector. Because the principal eigenvector approximates the true local tangent to the tract curve, tract propagation occurs in both collinear tangent directions approximated by $\pm\hat{v}_1(s)$. Tract propagation is subject to stopping criteria which include but are not limited to curvature,torsion, and local anisotropy metrics such as fractional anisotropy.

A notable variation of SLT known is the Tensor Deflection (TEND) algorithm [19]. The basis for the TEND algorithm is the use of the vector functional view of the entire diffusion tensor in Equation 1.10 to deflect the last streamline step direction $\hat{v}_1[n-1]$ to an updated step direction $\hat{v}_1[n]$. The motivation for TEND argued that a full tensor deflection approach to streamline tractography offered reduced directional

dispersion as a function of noise when compared to methods that follow the principal eigenvector. The TEND algorithm is also suggested to have greater ability to cross regions of planar diffusion tensors caused by intra-voxel orientational heterogeneity.

SLT based techniques suffer from an inability to infer crossing or branching tract structures. SLT techniques are unable to branch or join at tract crossings because of the implicit assumption that there is always one to one connectivity between a current point s_i and a next point s_{i+1} [27]. The work of [32] attempted to extend SLT to allow for branching and crossing by establishing propagation rules based on multi-voxel continuity metrics in forward mode until termination, then re-attempting tract traversal in reverse mode. Another extension of SLT that is capable of describing tract branching and crossing is the k-nearest neighbor approach [14]. The nearest neighbor method defines connectivity metrics according to distance between tensors, tensor shape, and tensor orientation, thereby inferring crossing and diverging connections within certain thresholds of crossing angles and voxel distances.

Current algorithm development in the area of DTI tractography has focused on the application of front propagation algorithms to the DTI tractography problem. Front-based tractography methods offer two advantages over SLT based methods. First, front propagation algorithms are capable of estimating branching and crossing tract structures in a more straightforward and computationally efficient manner than modified SLT techniques. Second, unlike SLT, front propagation algorithms estimate the likelihood of white matter connectivity between any two voxels.

For purposes of establishing necessary background, an outline of the the Fast Marching Tractography (FMT) algorithm developed by Parker et al. [27] will be provided. FMT is based on a fast marching level set method in which a front interface propagates in directions normal to itself with a non-negative speed function [24]. A time of arrival map is created for every point in a gridded space by recording the time at which the front passes each grid point. The relationship between time, T,

and speed, F, during front propagation is given by the Eikonal equation [30].

$$|\nabla T|F = 1 \qquad (1.15)$$

The FMT algorithm begins at the seed point with the consideration of the nearest neighbors around the seed point. In the 3-D case, the 6 nearest neighbors are defined as being in the Up, Down, North, South, East, and West Directions. A potential time of front arrival is assigned to each of the neighboring candidate points $p_1, p_2, p_3, p_4, p_5, p_6$ using Equation 1.16,

$$T(\mathbf{r}) = T(\mathbf{r}') + \frac{|\mathbf{r} - \mathbf{r}'|}{F(\mathbf{r})} \; , \qquad (1.16)$$

where $\mathbf{r}$ is a position vector specifying the grid location of a candidate point. The position vector $\mathbf{r'}$ describes the grid location of the closest point to $\mathbf{r}$ along the normal direction to the front, $-\hat{n}(\mathbf{r})$, that has already been passed by the front. The normal to the front may be calculated with 26 neighbor connectivity using Equations 1.17, 1.18, and 1.19.

$$\hat{n}(\mathbf{r}) = \frac{\nabla f(\mathbf{r})}{|\nabla f(\mathbf{r})|} \qquad (1.17)$$

$$\nabla f_x(\mathbf{r}) \approx \sum_{i=-1}^{i=1} \sum_{j=-1}^{j=1} \sum_{k=-1}^{k=1} C_i(r_x - i, r_y - j, r_z - z) \qquad (1.18)$$

$$C_{i,j,k}(r_x - i, r_y - j, r_z - k) = \begin{cases} i, j, k & : \; (r_x - i, r_y - j, r_z - k) \in \mathbf{S}(p) \\ 0 & : \; (r_x - i, r_y - j, r_z - k) \ni \mathbf{S}(p) \end{cases} \qquad (1.19)$$

In Equation 1.17, $\nabla f(\mathbf{r})$ is a concentration gradient of past band points that have already been passed by the front, f, as seen from a local candidate band position $\mathbf{r}$. The concentration gradient $\nabla f(\mathbf{r})$ is a vector composed of three Cartesian components: $\nabla f_x(\mathbf{r}), \nabla f_y(\mathbf{r})$, and $\nabla f_z(\mathbf{r})$. Equation 1.19 discretely approximates $\nabla f(\mathbf{r})$ using the concentration differences in the set of past band points, $\mathbf{S}(p)$, that have already passed by the front.
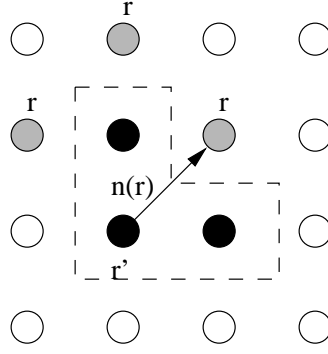
Figure 1.4: Two dimensional illustration of front propagation of FPT algorithm with four neighbor connectivity after two iterations. Points in past, candidate, and future bands are shown in black, gray, and white, respectively. The dashed line represents the propagation front. N($\mathbf{r}$) is normal to front from point $\mathbf{r}$

.

The seed point is considered to have already been passed by the front before the first iteration of the front propagation tractography algorithm. The speed function F($\mathbf{r}$) determines the speed of propagation from $\mathbf{r}$' to a candidate position $\mathbf{r}$. The candidate point with the fastest time of arrival, T($\mathbf{r}$), is selected as the next point of front arrival. The newest point is assigned a fixed time of arrival value T($\mathbf{r}$), and a fixed speed of arrival value F($\mathbf{r}$). The newest point of arrival at $\mathbf{r}$ is removed from the candidate band and is never considered again during propagation. Propagation continues as new times of arrival are calculated for points within the 6 point neighborhood of $\mathbf{r}$ that have yet to be reached by the front. Times of arrival for unselected candidate points are modified if the time of arrival for the current iteration is less than the time of previous iterations. Propagation continues until every point on the grid is assigned a time of arrival value. An illustration of the front propagation tractography algorithm described thus far is shown in Figure 1.4.

The FMT algorithm derives efficiency from the use of a min-heap data structure to locate the minimum time of arrival in the candidate band. An outline of the min-heap data structure as it is presented in [6] will now be provided along with the
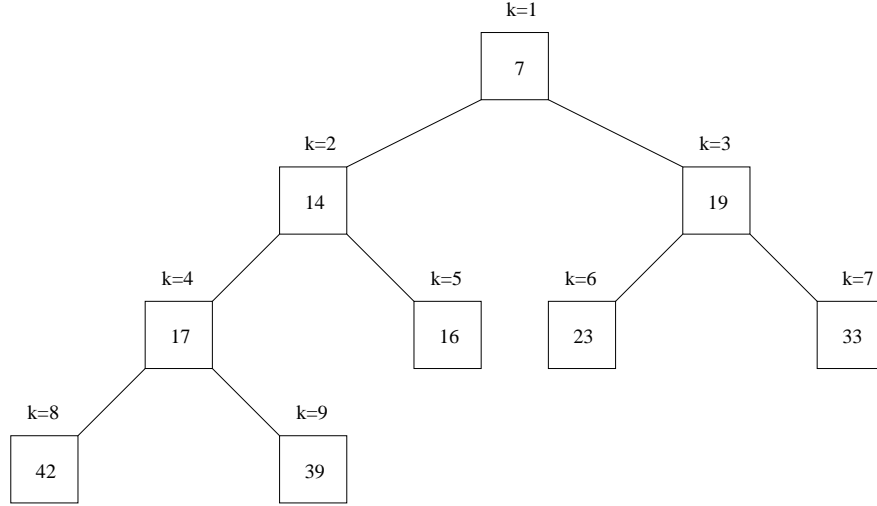
Figure 1.5: Illustration of min-heap data structure with nine elements.

modifications required for use in front propagation. A min-heap is a complete binary tree for which the value at any given parent node is less than or equal to the values of its children. It is most efficient to represent a heap data structure sequentially in memory as an array where a parent at location k has children defined at $2k$ and $2k + 1$. An illustration of a min-heap is provided in Figure 1.5.

The FMT algorithm requires three different operations on the min-heap: insertion, modification, and removal. Both insertion and removal and standard heap operations, while element modification is a special functionality of the heap required for front propagation. This discussion of the min-heap will cover all three heap operations.

Each time a new element is added to the candidate band, an insert into the min-heap must take place. Inserted elements are placed at the bottom of the heap and compared with the parent node. If the inserted element is smaller than its parent, the parent and the inserted element are swapped. The inserted element continues climbing the heap continues until the min-heap parent/child structure has been re-established. If there are M elements in the heap, an insertion requires $log_2(M)$ comparisons in the worst case.

A non-standard operation on the min-heap structure that is required for front

propagation is the modification of a point already in the candidate band of the front with a smaller trial time of arrival. Location of an existing element in the candidate band requires one operation assuming that each grid point has a back-pointer to the min-heap structure, otherwise $O(M)$ comparisons would be required to search for the modified candidate grid point in the heap. Once the trial time of a grid point is located and modified in the heap, the newly modified point must be allowed to climb the heap from its prior position K ($K \leq M$), requiring $log_2(K)$ comparisons in the worst case. Note that an updated point may only move up the min-heap because updates are only performed to assign lower times of front arrival to candidate points.

During front propagation, heap removal occurs when the fastest trial time is chosen from the candidate band. A removal begins by copying the current element at the top of the heap to a different location, taking the last element M at the bottom of the heap and placing it at the top of the heap. The smallest of the children at locations k=2 and k=3 are compared with the newly placed element at the top of the heap, and element swapping occurs if the element at the top of the heap is larger than its children. The element formerly at location M continues to descend the heap until the min-heap parent/child structure has been re-established, requiring $log_2(M)$ comparisons in the worst case.

The construction of past, candidate, and future bands made efficient by the use of the min-heap means that only points in the candidate band must be investigated during each iteration of front propagation. Ultimately, FPT requires $M^N log_2 M$ operations to assign time arrival values to all points on a N dimensional grid with M elements in each dimension [30].

The FMT algorithm uses the orientation and shape the diffusion tensor **D** to define the speed function F. The premise of FMT is that front propagation speed is controlled using **D** such that the front propagates fastest within white matter tracts. An example of a FMT speed function developed by Parker et al. [27] is included as

Equation 1.20,

$$F(\mathbf{r}) = min(F(\mathbf{r}'), |\hat{v}_1(\mathbf{r}') \cdot \hat{n}(\mathbf{r})|) , \qquad (1.20)$$

where the term $min(F(\mathbf{r}'))$ refers to the overall minimum historical speed of propagation to the point of the current iteration. The quantity $|\hat{v}_1(\mathbf{r}') \cdot \hat{n}(\mathbf{r})|$ is the absolute value of the scalar product between the principal eigenvector at the latest point accepted into the past band and the unit normal vector to the front from a candidate point at position $\mathbf{r}$. The term $|\hat{v}_1(\mathbf{r}') \cdot \hat{n}(\mathbf{r})|$ causes the front to propagate fastest in the direction of the principal eigenvector field. The use of a historical minimum speed is used to establish connectivity between the start point and all successive points of propagation.

In FMT, the time of arrival map from the seed point to other points in the DTI volume is used to construct minimum cost paths between the seed point and other points on the grid. Because diffusion tensor orientation is embedded in the time of arrival map, maximum speed paths from an end point to the seed point in a DTI volumes are estimates of white matter tract connectivity between the two points. Diverging tract structures may be inferred using FPT by constructing maximum speed tracts to the seed point using each point on the grid as a potential tract end point. In the process of traversing maximum speed tracts back to the seed point, some tracts will converge or cross, indicating the presence of crossing and diverging structure [27].

The likelihood metric capability of FMT allows for confidence estimates of white matter connectivity between any two points in a volume of DTI data [27]. Equation 1.21 is an example of a FMT likelihood function [27],

$$L(\gamma) = min(F(\gamma(s))) , \qquad (1.21)$$

where $\gamma(s)$ is a minimum cost tract between an end point and the seed point parameterized by s. Because the front propagates fastest inside regions of homogeneous diffusion tensor orientation, larger speeds over the extent of a tract indicate that a supposed tract is more likely to be a legitimate anatomical structure than an artifact.

The need to establish a gold standard of comparison by which to quantitatively compare tractography algorithms has been stressed in literature [10] [27]. To this point, published DTI phantom results have been limited to single tract experiments in which DTI data was obtained from co-registered diffusion weighted and T-2 images of manganese-enhanced rat optic tracts [13]. Quantitative comparisons were then made according to the angular deviation between planar tracts described in each image.

Chapter 2

Methods

2.1 Development and implementation of a streamline tractography algorithm

A basic streamline algorithm was implemented as a baseline measure with which to compare to the front propagation algorithm developed in Section 2.2. The framework of the streamline algorithm developed generally follows the Euler's method approach developed by Basser et al. [2]. The streamline discussion to follow provides specific implementation and thresholding design decisions within that framework.

The streamline approach to DTI tractography is based on the principle of creating a continuous approximation to a discretely sampled tensor field via interpolation. The continuous tensor field is then collapsed into a vector field based on the principal eigenvector direction $\hat{v}_1$ of the diffusion tensor $\mathbf{D}$. Streamline tractography approximates local tract orientation with the eigenvector, $\hat{v}_1$, associated with the largest eigenvalue of the diffusion tensor $\mathbf{D}$ starting from a seed point, r_0 [2].

$$
\begin{aligned}
\frac{d\mathbf{r}(s)}{ds} &= \hat{t}(s) \\
\hat{t}(s) &\approx \hat{v}_1(s) \\
\mathbf{r}(0) &= r_0 \\
T(\mathbf{r}) &= \mathbf{r}(s_0) + \alpha\hat{v}_1(s)
\end{aligned}
\tag{2.1}
$$

Tract propagation continues until one of the stopping criteria is met. These stopping criteria include anisotropy, curvature, eigensystem swap error, and grid boundary

24
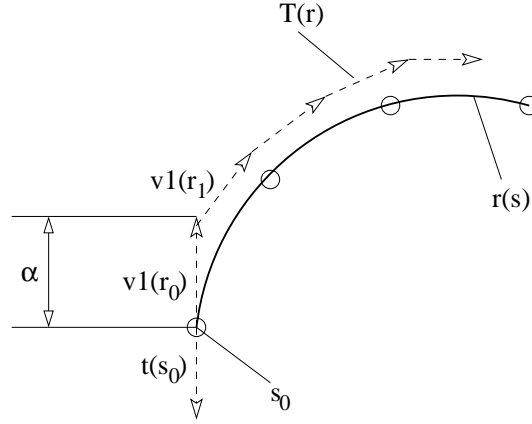
Figure 2.1: Illustration of streamline method. Tract approximation T($\mathbf{r}$) is based on taking linear steps of size α in direction of principal eigenvector $\hat{v}_1$. Streamline method is Euler's method approximation to curve where the principal eigenvector is assumed to approximate the tangent vector to the true tract curve $\mathbf{r}$(s).

conditions. An illustration of the streamline method is included as Figure 2.1

2.1.1 Interpolation of the diffusion tensor field

Given a discrete scalar field in a two dimensional space, a first order approximation to the scalar value at a continuous x, y location may be obtained through bilinear interpolation [29]. Bilinear interpolation of scalar value, $val(x, y)$, is simply the weighted average of the scalar values at known grid locations with values $val[x_i, y_i]$ based on the Euclidean distance from x, y to each of the known points. An illustration of bilinear interpolation is provided in Figure 2.2.

The concept of linear interpolation extends to a three dimensional space with six nearest known grid values $val[x_i, y_i, z_i]$ and an unknown value $val(x, y, z)$ at continuous location x,y,z. Equation 2.2 defines three-dimensional linear interpolation, or trilinear interpolation.

$$a = (x - x_1) \tag{2.2}$$
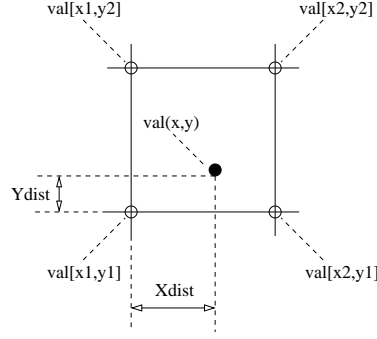
Figure 2.2: Bilinear interpolation. Value at a continuous location $val(x, y)$ is weighted average of known discrete grid values $val[x_i, y_i]$. Weight of each $val[x_i, y_i]$ is Euclidean distance to desired (x, y) point. The grid value $val[x_1, y_1]$ contributes to $val(x, y)$ with a weight determined by $w = \sqrt{Xdist^2 + Ydist^2}$, defined as the Euclidean distance between (x, y) and $[x_i, y_i]$

$$b = (y - y_1)$$
$$c = (z - z_1)$$

$$val(x, y, z) =$$
$$(1-a)(1-b)(1-c)val[i, j, k] + (a)(1-b)(1-c)val[i+1, j, k] +$$
$$(a)(b)(1-c)val[i+1, j+1, k] + (1-a)(b)(1-c)val[i, j+1, k] +$$
$$(1-a)(1-b)(c)val[i, j, k+1] + (a)(1-b)(c)val[i+1, j, k+1] +$$
$$(a)(b)(c)val[i+1, j+1, k+1] + (1-a)(b)(c)val[i, j+1, k+1]$$

The continuous eigensystem information required for the streamline method was obtained using trilinear interpolation of the diffusion tensor field. Each of the six unique elements, D_i of the diffusion tensor $\mathbf{D}$ were interpolated separately. Because differential equations were not used for streamline tract estimation, the first order accuracy in $\mathbf{D}$ estimates provided by trilinear interpolation was sufficient. Smoother tract estimates would result from the use of second order spline interpolations of $\mathbf{D}$,

but tract smoothness would not be based on any more measured information.

In general, the continuous eigensystem information required during streamline propagation may also be obtained from DWI interpolation or eigensystem interpolation. Starting from the level of DWI data requires the interpolation of each diffusion weighted measurement S_i where $i \geq 6$, followed by a regression estimate of $\mathbf{D}$ using the Stejskal-Tanner equation, followed by diagonalization to find the eigensystem information of interest. It should be noted that because the Stejskal-Tanner equation is non-linear, interpolation estimates obtained from DWI and DTI data are are not equivalent, although it has been experimentally shown that DWI and DTI interpolation yield similar tractography estimates [15]. A complete eigensystem interpolation requires the interpolation of the 12 eigenvector/eigenvalue elements, although only 6 eigensystem elements are required (PEV and three eigenvalues) if no torsion constraints are desired during SLT propagation. Although eigensystem interpolation is possible, it is complicated by the lack of correspondence between neighboring eigensystems [15]. DTI interpolation was adopted to avoid the computational burden associated with DWI interpolation, and to avoid the greater complexity associated with eigensystem interpolation.

2.1.2   Streamline propagation and stopping criteria

Estimation of white matter structure was accomplished using the Euler's method streamline approach starting at a seed point and following the principal eigenvector $\hat{v}_1$ of the diffusion tensor in step sizes $0 \leq \alpha \leq 1$. Following the recommendation of [3], the choice of α was left as a functional input to the streamline algorithm in order to allow for a value of α to be found such that tract estimation converged to a stable and reproducible result. In [3], step sizes $\alpha < 0.05d$ were proposed as being sufficient for most streamline applications, with d equal to an isotropic voxel dimension. In the tractography experiments conducted in this research, a larger Euler's method step size of $\alpha \leq 0.1$ was usually sufficient to obtain tract estimate convergence.

Because the streamline algorithm developed in this research used a discrete integer coordinate system: $X \in [0, M], Y \in [O, N], Z \in [0, P]$, with M, N and P integer and greater than zero, different step sizes had to be enforced in the case of non-isotropic spatial sampling. Take for example a clinically realistic case in which DWI measurements are taken at a resolution of 1 mm x 1 mm x 3 mm within a cubic field of view. In this case, using the same step size in and out of plane would result in steps 3 times as large in plane as out of plane in physical space. In order to ensure steps of uniform physical length, an out of plane step size one-third that of the in-plane step size would be required. Using the reasoning of the previous example, a step size correction was implemented such that the step length in each of the three principal directions, $\hat{x}, \hat{y}, \hat{z}$, was normalized according to the dimension of poorest resolution.

Because the principal eigenvector of the diffusion tensor $\mathbf{D}$ defines two co-linear step directions $\pm\hat{v}_1$, tract propagation must start from the seed point in both forward and backward directions. Forward tract propagation must consistently follow $+\hat{v}_1$ step directions, and backward tract propagation must consistently follow the $-\hat{v}_1$. Enforcing a consist signage on the step direction defined by the principal eigenvector direction prevents tract propagation from bouncing back and forth along the same tract region $T(\mathbf{r_i})$.

The first of the stopping criteria used to halt the propagation of streamline tracts was maximum tract curvature. The curvature threshold enforced a tract continuity constraint based on a biological argument that white matter tracts do not bend sharply within the mm distance of DWI imaging voxels [32]. A maximum curvature threshold was computed using the angular deviation between successive step directions $\hat{v}_1(\mathbf{r_{i-1}})$ and $\hat{v}_1(\mathbf{r_i})$, where $\mathbf{r_i}$ is the position of the current tract point that was reached by stepping in direction $\hat{v}_1(\mathbf{r_{i-1}})$ from the previous tract point $\mathbf{r_{i-1}}$. The angular deviation between step directions was computed using the definition of the dot product.
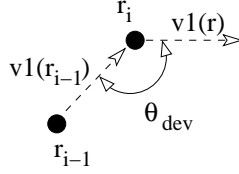
Figure 2.3: Illustration of angular deviation metric between successive steps of streamline tract propagation

$$\theta_{dev} = |cos^{-1}(\hat{v}_1(\mathbf{r_{i-1}}) \cdot \hat{v}_1(\mathbf{r_i}))| \tag{2.3}$$

In Equation 2.3, the hat notation of the principal eigenvector directions $\hat{v}_1$ reflects that $\hat{v}_1$ vectors are unit vectors. An illustration of the angular deviation curvature metric described in Equation 2.3 is shown as Figure 2.3.

Using the absolute value of local angular direction between the previous step direction and the current candidate step direction, the curvature threshold was implemented by comparing the angular deviation resulting from the current candidate Euler's method step to a threshold value. If θ_{dev} exceeded $K_{threshold}$, propagation of the current tract ceased and a step in direction $\hat{v}_1(\mathbf{r_i})$ was not taken. Because the underlying structure of the tracts being estimated in tractography is unknown, there is no ground truth by which to set a maximum tract curvature threshold. Therefore, a $K_{threshold}$ value was selected in a trial and error visual inspection process by varying $K_{threshold}$ until heterogeneously oriented tracts of large curvature were eliminated. A curvature threshold of 45 degrees generally produced anatomically reasonable results in human data sets. The widely accepted range of $K_{threshold}$ values in literature is somewhere in the neighborhood from 90 to 45 degrees.

The second stopping criteria used to halt propagation of streamline tracts was an eigensystem sorting error condition. As mentioned in Chapter 2, streamline methods are subject to sorting errors in which noise perturbs the eigenvalues of $\mathbf{D}$ such that a principal eigenvector direction $\hat{v}_1$ is selected, when in reality one of the eigenvectors

$\hat{v_2},\hat{v_3}$ with lesser eigenvalues λ_2, λ_3 is a more accurate estimate of local tract orientation [2]. Sorting errors were detected using the angular deviation metric of the form described in Equation 2.3 with the previous accepted step direction $\hat{v_1}(\mathbf{r_{i-1}})$. At each iteration of streamline propagation, angular deviations were computed between the previous principal eigenvector direction $\hat{v_1}(\mathbf{r_{i-1}})$ and each of the eigenvectors of $\mathbf{D}$ at the current location. If the angular deviation between either of the non principal eigenvectors at the current location $\hat{v_2}(\mathbf{r_i}), \hat{v_3}(\mathbf{r_i})$ and the eigenvector at the last accepted tract point $\hat{v_1}(\mathbf{r_{i-1}})$ was less than the angular deviation between $\hat{v_1}(\mathbf{r_i})$ and $\hat{v_1}(\mathbf{r_{i-1}})$, an eigensystem sorting error flag was set and propagation ceased.

The third stopping criteria used to halt propagation of streamline tracts was insufficient diffusion tensor anisotropy. In regions of homogeneous, highly anisotropic white matter, the principal eigenvector direction followed by the streamline method is a good approximation of local tract structure. Because tractography algorithms have no knowledge of local tract orientational homogeneity, validity of orientational maximum described by the tensor model can only be inferred through tensor anisotropy. A common metric of tensor anisotropy is fractional anisotropy, shown in Chapter 1 as Equation 1.12. For FA values greater below some threshold, it was assumed that streamline tract estimates were not based on a sufficient level of confidence in the tract orientation approximation given by the principal eigenvector of $\mathbf{D}$, and tract propagation ceased. As in the case of curvature thresholding, there are no biologically verified FA limits at which the principal eigenvector of $\mathbf{D}$ ceases to accurately describe local tract structure. Selection of proper $FA_{threshold}$ values was accomplished by trial and error by varying $FA_{threshold}$ values until tracts of excessive length and curvature were eliminated in benchmark sections of the brain such as the corpus callosum. Within the data sets explored, $FA_{threshold}$ values in the range 0.1-0.4 provided anatomically reasonable results.

The FA threshold also enforced the final stopping criteria used in the streamline algorithm: the grid boundary. Because DWI data collected outside the volume of

interest is meaningless, the streamline algorithm received a data mask as input that limited tractography consideration to the region within the volume interest. Although automated brain extraction algorithms could have been implemented, masks were obtained in practice by manually tracing around the skull of each non-diffusion weighted axial slice of a DWI volume. Points outside the binary mask were assigned diffusion tensors with all zero elements, resulting in FA values of zero. Because the volume of interest always lied within the grid boundary, the FA threshold provided a means of ensuring tractography results stayed within the physically meaningful section of the grid boundary.

2.2 Development and implementation of the front propagation tractography algorithm

Following the framework of the Fast Marching Tractography (FMT) algorithm developed by Parker et al. [27], the Front Propagation Tractography (FPT) algorithm consists of three functional components: Front propagation from a seed point, connectivity estimation within a time of arrival map, and likelihood estimation of potential tracts. Front propagation is a mechanism for embedding white matter connectivity information in a diffusion tensor field into a scalar time of arrival field. Once connectivity information is encoded into the form of a scalar field, a discrete network approach is applied to provide tract connectivity estimates. Finally, the likelihood of a tract is determined based on the concept that propagation speed is related to confidence in the tensor model. A high level view of front propagation tractography is shown as Figure 2.4.

2.2.1 Front propagation

The forward propagation scheme used the standard FMT min-heap/grid approach described in Chapter 1. Interconnectivity between the min-heap and the grid was
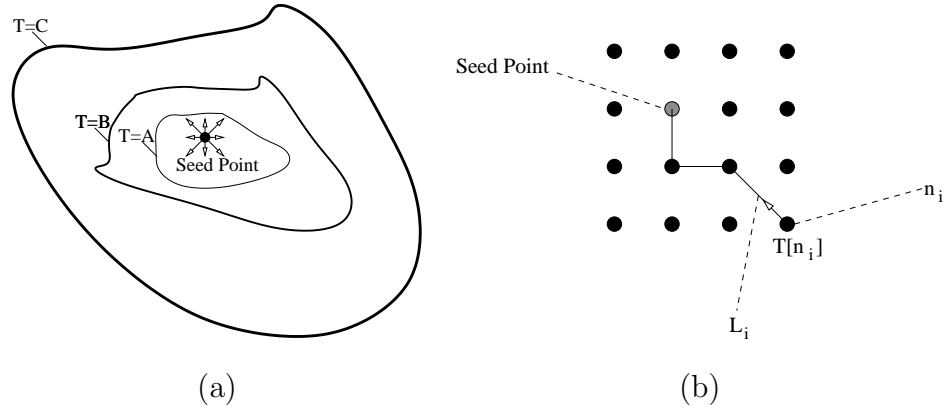
Figure 2.4: High level view of front propagation tractography algorithm (a) Outward propagation and time of arrival assignment (b) Network connectivity between end points n_i and seed point. Closed contours represent time isobars in which $A < B < C$. L_i is likelihood of tract between seed point and end point n_i. $T[n_i]$ is time of arrival assigned to each network node during outward propagation of (a).

established via storage of the grid index corresponding to each narrow-band point in the heap, and likewise the storage of corresponding heap indexes in each element of the grid. The Grid was created as an array of Grid Elements. Grid Elements were defined as three element structures containing arrival time, arrival speed, and heap index information. The heap index of a grid element described the location of that grid element in the heap. The Min-heap was implemented using a single dimensional array of Heap Elements. Heap Elements contained X,Y,Z Cartesian points referencing the location of the Heap Element in the Grid. A graphical description of the data structures described in this paragraph appear in Figure 2.5.

In order to verify the construction the forward propagating front, a constant speed function of F=1.0 was used to radiate a front away from a source point. The result of this verification step is shown graphically in Figure A.1. Viewing Figure A.1, it can be noted that a roughly circular wavefront advances away from the source point in a monotonically increasing fashion. An interesting feature of the time isobars of A.1 is the octagonal geometry of what should ideally be circular propagation. The

MinHeap

| Heap Element 1 |
| Heap Element 2 |
| Heap Element N |

Heap Element

| X |
| Y |
| Z |

(a)

Grid

GridPoint 1,1	GridPoint 1,2	GridPoint 1,N
GridPoint 2,1	GridPoint 2,2	GridPoint 2,N
GridPoint M,1	GridPoint M,2	GridPoint M,N

Grid Point

| Arrival Time |
| Arrival Speed |
| Heap Index |

(b)
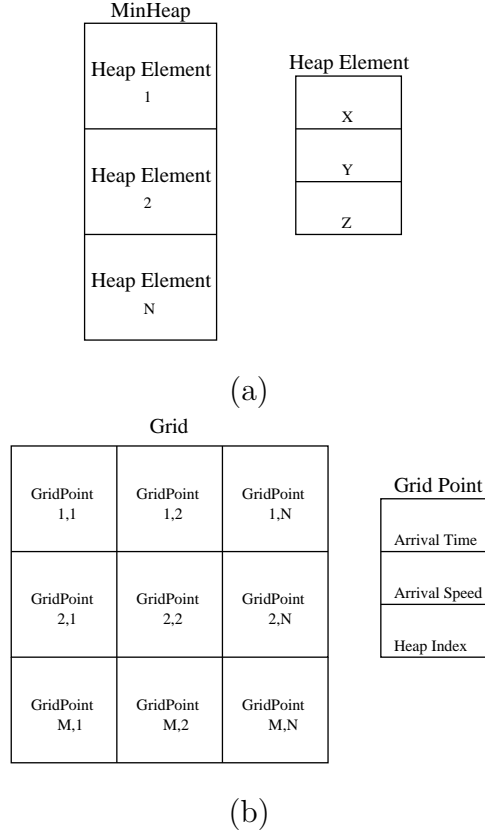
Figure 2.5: Data structures (a) Min-Heap (b) Grid

octagonal geometry of radiation is an artifact of the eight point connectivity used during forward propagation. The octagonal geometry of propagation can be noted in the intensity plot as a star-like artifact in which the front propagation is faster along directions of connectivity. The connectivity artifact seen in this example also occurs during FPT propagation with non-constant speed functions, the effect of which will be discussed in subsequent sections of this thesis.

2.2.2 Defining the front propagation speed function

This thesis explored a new definition for a speed function F for use in FPT front propagation. The speed function was defined using the concept of an average value normalized orientation density function $\text{ODF}(\mathbf{r},\hat{u})$ [8]. The orientation density func-

tion $ODF(\mathbf{r}, \hat{u})$ provides weighted estimates of the likelihood of diffusion in a unit vector direction $\hat{u}$ at a particular location in a DTI volume given by the position vector $\mathbf{r}$. The ODF developed to govern propagation speed is listed as Equation 2.4,

$$ODF(\mathbf{r}, \hat{u}) = \frac{\hat{u}^T \mathbf{D} \hat{u}}{< ODF(\mathbf{r}, \hat{u}) >} \ , \tag{2.4}$$

where the quantity $\hat{u}^T \mathbf{D} \hat{u}$ is the directionally dependent portion of the signal loss exponent in the Stejskal-Tanner model used to construct the diffusion tensor, which was shown previously in Equation 1.4. In the Stejskal-Tanner model, a series of DWI measurements taken in a finite number of measurement directions $\hat{u}_i$ is used to calculate a regression estimate of a diffusion tensor $\mathbf{D}$ that models the magnitude and direction of diffusion over a continuous angular space in any unit vector direction $\hat{u}$. Once the diffusion tensor is estimated using the Stejskal-Tanner model, an estimate of the probability of diffusion in any direction $\hat{u}$ may be obtained by re-applying the Stejskal-Tanner model with a knowledge of $\mathbf{D}$. Thus, the ODF defined in Equation 2.4 is a regression estimate of the likelihood of diffusion in a direction $\hat{u}$ based on the diffusion tensor model.

The quantity $< ODF(\mathbf{r}, \hat{u}) >$ in Equation 2.4 is the average value of the ODF at a location $\mathbf{r}$ calculated over the infinite set of unit vector directions. In practice, $< ODF >$ was approximated using an isotropically sampled set of directions $\hat{u}_N$, where $N = 26$ was selected to match the connectivity between $\mathbf{r}$ and $\mathbf{r}'$ imposed during outward propagation. Normalizing the ODF estimate of diffusion in a direction $\hat{u}$ by the average value of the ODF creates an anisotropy boundary at $ODF(\hat{u}) = 1$. In the case of isotropic diffusion, the normalized ODF takes on a value of 1 in any measurement direction, since diffusion is equally probable in all directions. In a region of anisotropic diffusion, likelihood of diffusion given by the ODF is less than average in directions misaligned with the orientational maximum of the diffusion ellipsoid, and greater than average in directions aligned orientational maximum of the diffusion ellipsoid.

As diffusion becomes more highly anisotropic, the disparity between ODF values for directions orthogonal and parallel to the orientational maximum of the diffusion ellipsoid becomes higher, narrowing the band of directions for which the ODF has a value greater than one, and increasing the values output by the ODF for directions aligned with the orientational maximum. The set of directions $\hat{u}_i$ for which $ODF(\hat{u}_i)$ attains a value greater than one represents a solid angular band within which there is a better than average probability of diffusion in the direction $\hat{u}_i$.

The speed function $F(\mathbf{r}, \hat{n}(\mathbf{r}))$ used in the FPT algorithm to propagate the front was defined in terms of two piecewise intervals using the normalized ODF of Equation 2.4.

$$F(\mathbf{r}, \hat{n}(\mathbf{r})) = \begin{cases} ODF(\mathbf{r}', \hat{n}(\mathbf{r})) & : & ODF(\mathbf{r}', \hat{n}(\mathbf{r})) > 1 \\ 0 & : & ODF(\mathbf{r}', \hat{n}(\mathbf{r})) \leq 1 \end{cases} \tag{2.5}$$

The speed function F was defined in terms of a normalized orientation density function for two purposes. First, front evolution ought to be directionally limited to reflect the anisotropy of the diffusion tensor field. As discussed in the literature review, it has been experimentally verified that in this case of isotropically oriented highly anisotropic white matter, the orientational maximum of the diffusion tensor given by the principal eigenvector is a good estimate of local tract orientation. When the tensor model is an accurate estimate of white matter orientation, it is desirable to evolve the front interface such that the front evolves in the direction indicated by the orientational maximum of diffusion tensors in the past band. Because a high degree of confidence exists that the orientational maximum of a point in the past band at $\mathbf{r}'$ reflects the orientation of a white matter tract, only points in the direction of the orientational maximum at $\mathbf{r}'$ ought to be considered for front arrival.

Looking at the definition of Equation 2.5, propagation is restricted to the band of directions for which $F(\mathbf{r}, \hat{n}(\mathbf{r}))$ is greater than one. Higher degrees of anisotropy in the tensor at $\mathbf{r}'$ decrease the set of candidate points for which F($\mathbf{r}$) will evaluate to non-

zero values, thereby focusing the candidate band to a small set of points well aligned with the higher confidence orientation estimate provided by the diffusion tensor. In Figure A.2, the orientation density function $ODF(\mathbf{r}', \hat{n}(\mathbf{r}))$ was projected onto a unit sphere for the case of a highly anisotropic diffusion tensor at $\mathbf{r}'$. Figure A.2 illustrates the point that in regions of homogeneously oriented, anisotropic tensors, propagation is restricted to a narrow band of angular directions that are aligned with the local tensor orientation. The angular band of allowed propagation directions is represented by unit vector directions from the origin to the surface of the unit sphere for which the surface intensity is non-zero.

The ODF construction used to formulate the speed function in this research is similar in nature to the example speed function proposed by Parker et al. listed as Equation 1.20. As in Equation 2.5, speeds in the formulation of Equation 1.20 are weighted based on the alignment with the candidate points and the diffusion tensor orientation in the past band. The advantage of the ODF construction is that in the case of propagation within a highly organized, anisotropic white matter tract, points adjacent to the current tract are never assigned time of arrival values. This focused propagation is appropriate since the orientational maximum of the diffusion tensor is a valid estimate of local white matter orientation. Reducing the window of evolution of the front reduces the computational burden of adding points to the candidate band for which there is no evidence of connectivity to the current tract. As an aside, it can be noted that in the limit as $\mathbf{D}$ degenerates into a line with complete anisotropy, the propagation windowing of the speed function of Equation 2.5 effectively reduces the front propagation tractography algorithm to a basic streamline tractography algorithm.

In regions where the tensor model begins to break down due to intra-voxel orientational heterogeneity, which is indicated by a reduction in anisotropy of the diffusion tensor, it is desirable to propagate the front in a large range of directions in order to allow the TA map to evolve in a diverging manner. Divergence in the TA map cre-

ates the possibility for crossing and diverging tracts to be detected during a backward search of the time of arrival map. The ODF construction of the speed function also provides confidence based front propagation behavior. Another unit sphere projection of the ODF function is included in Figure A.3 to illustrate the broadening of the propagation focus imposed by the speed function in cases of lower anisotropy. Looking at the Figure A.3, it is apparent that the angular window of allowed propagation directions has widened compared to Figure A.2.

A second advantage of the speed function of Equation 2.5 is that the range of possible propagation speeds reflects confidence in the validity of the tensor model as suggested by the anisotropy of **D**. Weighting propagation speed based on tensor anisotropy supports the use of speed governed tract likelihood functions. In the speed function of Equation 2.5, tensors with a higher degree of anisotropy yield a higher upper limit of front propagation speeds than those of lower anisotropy. Thus, propagation is defined in terms of the complete set of tensor information: orientation and geometry. In cases of highly anisotropic tensors, propagation only occurs in the direction of the orientational maximum and it occurs at a relatively high rate of speed. In the case of more isotropic diffusion tensors, propagation slows as the window of propagation directions is widened. The speed dependence on anisotropy described in this paragraph is reflected in Figures A.2 and A.3. The color-bars of the spherical projections of the ODF indicate that higher propagation speeds result from tensors with higher levels of anisotropy.

The performance of the speed function of Equation 2.5 stands in comparison to the speed function of Equation 1.20, in which propagation speeds are restricted between the same zero to one range regardless of the degree of confidence in the tensor model reflected by anisotropy. This failure to directly include anisotropy information within the speed function can lead to sorting bias in cases when the principal eigenvector is only slightly bigger than the second biggest eigenvector/eigenvalue pair. In this case, there is little confidence as to where propagation should occur plane defined by

$\hat{v}_1, \hat{v}_2$, yet Equation 1.20 allows propagation to occur only in the $\hat{v}_1$ direction despite a low degree of confidence in the orientational information given by the diffusion tensor model. The approach of 1.20 could be improved by adding FA to the list of minimum worst case decisions, however, this approach would still be inferior to that of Equation 2.5 due to the loss of connection between anisotropy and orientation information that is inherent in diagonalization of the diffusion tensor.

2.2.3 Connectivity estimates

In the FMT algorithm developed by Parker et al. [27], connectivity estimation was obtained through gradient descent on a continuous interpolated scalar field. In the proposed FPT algorithm, a discrete network approach is used to construct tract connection estimates. Each of the points in the time of arrival map are viewed as network nodes, n, with node costs, c. The maximum likelihood estimate of connection between any two points is then the minimum cost path within the discrete connectivity of the time of arrival map.

$$T(\mathbf{r}) = min_\gamma C(\gamma[n_i]) \qquad (2.6)$$

Equation 2.6 states that the tract $T(\mathbf{r})$ between two points M and N is the tract for which the cost function C is minimized with respect to all possible paths γ containing i nodes n_i. The cost function C is determined by the sum of node costs c accrued along path γ.

$$C(\gamma[n_i]) = \sum_{k=1}^{k=i} c_k \qquad (2.7)$$

A simplifying observation in constructing connectivity estimates within the time of arrival grid is that the time of arrival grid is a monotonically increasing function with respect to distance from the seed point M. The monotonic nature of the time of arrival grid TA means that from an end point N, a path between M and N can be found by repeatedly taking discrete steps in the direction for which the TA gives the lowest

time of arrival value. This approach of blindly following a local minimum/maximum is known as a greedy search. Because the greedy search only looks within a limited neighborhood of local connectivity to determine a minimum cost estimate within a network, it is a local estimate of minimum cost, and is therefore only an approximation to the global maximization phrasing of Equations 2.6 and 2.7.

Because speed, not time, is the indicator of connectivity likelihood in the front propagation formalism, construction of minimum cost tract estimates was achieved by weighting nodes within the time of arrival network such that node costs c_j reflected propagation speed. From a point i in the time of arrival map, costs were assigned to all neighboring points j according to Equation 2.8,

$$c_j = TA[j] \cdot |j - i| \, , \tag{2.8}$$

where TA[j] is the time of arrival at neighboring location j and $|j-i|$ is a speed weight given the Euclidean distance between j and i. The weighting term $|j-i|$ imposes higher costs on time points further from the present location i, thereby creating a network in which greedy cost paths reflect greedy maximum speed paths between any two points j and i. The greedy search described in Equation 2.8 was limited to a 26-neighbor region of connectivity in order to match the connectivity used during outward front propagation. A pseudo-coded description of the greedy search algorithm described in this section is included as Algorithm 1.

2.2.4 Likelihood estimates

As discussed in the front propagation section, the ODF construction of the speed function embeds confidence information in terms of speed during propagation of the front interface. Higher speeds of arrival in points r_i of a FPT tract estimate $T[r_i]$ reflect regions of higher anisotropy and higher orientational homogeneity, and therefore higher confidence in the tensor model used to obtain connectivity estimates. Therefore, higher likelihood estimates should be given to tracts for which front propagation

---

Algorithm 1 Greedy Search

Initialize current point to end point

Initialize weight(i) to all distances in i point connectivity

Initialize stepDirections(i) to all neighbor directions in i point connectivity

while current point $\neq$ seed point **do**

  minCost=Cost(currentPoint)

  for i=1:numNeighbors **do**

    nextPoint=currentPoint+stepDirection(i)

    currentCost=weight(i) $\cdot$ TA(currentPoint+stepDirection(i))

    if $currentCost < minCost$ **then**

      nextPoint=currentPoint+stepDirection(i)

      timeMin = TA(nextPoint)

    end if

  end for

  Store nextPoint into TRACT

  currentPoint=nextPoint

end while

---

occurred relatively fast, and lower likelihood estimates should be given to tracts in which front propagation occurred at a relatively slow rate [27].

A second consideration in the selection of a likelihood estimate is the effect of the likelihood estimate on the ability of the FPT algorithm to estimate diverging tract structure. The ODF based speed function used to advance the front reduces propagation speed in regions of low anisotropy. Because fiber crossings reduce the anisotropy of the tensor model, small regions of low anisotropy may reflect crossings. Overly penalizing tracts built from points with the occasional low speed of arrival therefore limits the ability of FPT to detect fiber crossings.

The likelihood function used in the FPT algorithm of this research was the arithmetic mean of the individual speeds of front arrival, SA, at each point along a potential tract, $\mathbf{r_i}$.

$$L(T(\mathbf{r})) = \frac{\sum_{i=1}^{i=n} SA[\mathbf{r_i}]}{n} \tag{2.9}$$

The likelihood function of Equation 2.9 provides the average speed of propagation along a n point tract between an end point N and a seed point M. Potential tracts with higher average speeds receive a greater estimate of likelihood than those with lower average speeds. The arithmetic average of propagation speeds does not over-penalize likelihood estimates for tracts composed of points with infrequent low speed of arrival values, as in the worst case minimum speed of propagation definition proposed by Parker et al. in Equation 1.21. The likelihood function of Equation 2.9 trades increased ability to detect fiber crossings with increased likelihood of false positive tract estimates compared to Equation 1.21. Because the basis for using more advanced front propagation tractography methods over streamline methods is to allow for the detection of crossing and diverging structure, it seemed reasonable to trade increased ability to resolve IVOH for increased false positive tract artifacts.

Once likelihood estimates were computed for all connections within a volume of interest, an Nth percentile threshold was used to select tracts within an N percent level

of confidence, as was done in the FPT algorithm developed in [27]. Because potential tracts between different seed and end points may be composed of the same sample points **r**, the likelihood estimates of different tracts are not statistically independent samples. Therefore, the central limit theorem does not apply and a Gaussian distribution can not be assumed for a large number of L values within a volume. Without the central limit theorem or any *a-priori* information regarding underlying statistical distribution of L, the threshold between invalid and valid FPT tract estimates must be made without assuming any form of the distribution of L. Using a Nth percent threshold based on L values of potential tracts is a reasonable means of separating valid and invalid tract estimates since Nth percent thresholding does not assume any form for the distribution of L.

2.3 Generation of a software DTI phantom

2.3.1 Parameterization of desired tracts

Two types of synthetic tract geometries were generated for use in this research. Linear tracts were created in the interest of studying the performance of tractography algorithms in cases of low curvature. The second tract geometry synthesized for use in this study was a helix. A helical geometry was selected in the interest of examining the performance of DTI tractography algorithms in tracts with both in plane and out of plane curvature. Both the position and tangent equations for a line and helix are easily parameterized. The parameterized position and tangent equations for a line are shown in Equations 2.10 and 2.11

$$
\begin{aligned}
r_x(t) &= x_0 + At \\
r_y(t) &= y_0 + Bt \\
r_z(t) &= z_0 + Ct
\end{aligned}
\tag{2.10}
$$

$$v_x(t) \quad = \quad A \tag{2.11}$$
$$v_y(t) \quad = \quad B$$
$$v_z(t) \quad = \quad C$$

The position and tangent equations for a helix are shown in Equations 2.12 and 2.13.

$$r_x(t) \quad = \quad k_1 cos(t) \tag{2.12}$$
$$r_y(t) \quad = \quad k_1 sin(t)$$
$$r_z(t) \quad = \quad k_2 t$$

$$v_x(t) \quad = \quad -k_1 sin(t) \tag{2.13}$$
$$v_y(t) \quad = \quad k_1 cos(t)$$
$$v_z(t) \quad = \quad k_2$$

From basic calculus, the tangent equations in Equations 2.11 and 2.13 may be obtained from the position equations by taking the derivative with respect to t of the parameterized position equations. The constants A, B, and C in Equation 2.10 represent the slope of the line in the x, y, and z directions. In Equation 2.12, the constant k_1 determines the radial size of the helix. The constant k_2 controls the z rate of change of the helix.

2.3.2   Steering the diffusion tensor orientation

The creation of software phantoms required the ability to construct diffusion tensors with eigensystems pointing principally in the direction of desired structure. Specification of tensors with desired $\hat{v}_1$ eigenvector orientations was accomplished using an

eigenvector/eigenvalue decomposition, as shown in Equation 2.14.

$$\mathbf{D} = \lambda_1 \hat{v}_1 \hat{v}_1{}^t + \lambda_2 \hat{v}_2 \hat{v}_2{}^t + \lambda_3 \hat{v}_3 \hat{v}_3{}^t \tag{2.14}$$

In order to obtain symmetric tensors, it was necessary to specify two other eigenvectors, $\hat{v}_2$ and $\hat{v}_3$, that defined an orthonormal basis along with the principal eigenvector. Since no torsion constraints were placed on either the streamline or the fast marching algorithms of Chapters 2 and 3, $\hat{v}_2$ and $\hat{v}_3$ directions normal to both each other and the principal eigenvector direction were selected arbitrarily from the infinite set of possible solutions. Given a desired principal direction of diffusion direction $\hat{v}_1$, Equation 2.15 was chosen to constrain $\mathbf{\hat{v}_2}$ such that $\hat{v}_1 \cdot \hat{v}_2 = 0$.

$$\mathbf{\hat{v}_2} = \frac{1}{v_{1x}} \hat{i} - \frac{2}{v_{1y}} \hat{j} + \frac{1}{v_{1z}} \hat{k} \tag{2.15}$$

A system of three independent linear equations Ad=s in three unknowns was then built and solved to constrain $\hat{v}_3$ to an orthonormal basis given $\hat{v}_1$ and the v_2 selected by Equation 2.15. The linear system constraining $\hat{v}_3$ was built from the conditions: $\hat{v}_1 \cdot \hat{v}_3 = 0$, $\hat{v}_2 \cdot \hat{v}_3 = 0$, $\hat{v}_1 \times \hat{v}_3 = \hat{v}_2$.

$$\begin{bmatrix} 0 & v1_z & -v1_y \\ -v1_z & 0 & v1_x \\ v1_y & -v1_x & 0 \end{bmatrix} \begin{bmatrix} v3_x \\ v3_y \\ v3_z \end{bmatrix} = \begin{bmatrix} v2_x \\ v2_y \\ v2_z \end{bmatrix} \tag{2.16}$$

Because the choice of $\hat{v}_2$ in Equation 2.15 is undefined for $\hat{v}_1$ components of zero, two cases for which $\hat{v}_1$ components came within a threshold $t = 0.001$ of zero where treated as special cases. In the event two of the components of $\hat{v}_1$ fell inside t, $\hat{v}_2$ and $\hat{v}_3$ were each assigned a value of one of the directions following within the threshold. The following process was used in the case that one component of v_1 was near zero, where for discussion purposes assume the near zero component is $v1_x$. In this case, $\hat{v}_2$ was assigned by normalizing $\mathbf{\hat{v}_2} = 0\hat{i} - v1_z\hat{j} + v1_y\hat{k}$ and $\hat{v}_3$ was assigned to $\hat{v}_3 = 1\hat{i} + 0\hat{j} + 0\hat{k}$. The method just described follows for the case of near zero y or z components.

The next step in using the Eigenvalue decomposition of Equation 2.14 was the selection of Eigenvalues. Eigenvalue weights λ_1, λ_2, and λ_3 were assigned such that the eigenvalues of the synthetic data were similar in scale to the values noted in white matter tracts of real human brain DTI data. Values for λ_1, λ_2, and λ_3 were fixed at 0.001, 0.0003, and 0.0003, respectively. The chosen eigenvalue weights correspond to a FA metric of, which is also typical of FA encountered in human data in highly anisotropic regions such as the corpus callosum.

2.3.3 Defining a diffusion tensor field

The first task in defining a diffusion tensor field was defining the tract boundary. In the synthetic data sets, tracts were assumed to have a circular cylindrical geometry with radius r. From basic geometry, the intersection of a right circular cylinder at an angle to a plane forms an ellipse. Thus, linear tracts formed elliptical areas when they intersected an axial plane. The area formed by the intersection of helical tracts passing through each axial slice was also modeled as an ellipse. This first order approximation to the axial plane intersection area of the ellipse ignored the effect of curvature during intersection. The position of the center of the tract intersection at each axial plane was given by the parameterized position equation of the desired tract geometry. The orientation of the semi major axis of the intersection ellipse was given by the orientation of the x and y components of the parameterized tangent equation of interest. The size of the semi minor axis of the intersection area was set equal to the radius of the tract cylinder. The formula governing the size of the semi-major axis of the intersection ellipse at an angle θ from the normal to the axial plane is given in Equation 2.17.

$$r_1 = \frac{r}{cos(\theta)} \tag{2.17}$$

Once the boundary of the tract was established in each slice, the formation of a coherently organized fiber tract was straight forward. For each axial slice, all points within the elliptical area of tract intersection were assigned a diffusion tensor oriented

in the tangent direction to the helix at that slice. The linear and helical tensor fields resulting from the process described to this point are represented in terms of diffusion Ellipsoids in Figure A.4. Points outside tract boundaries were assigned homogeneous tensors of uniformly random orientation and FA values of zero. The presence of uniformly oriented homogeneous tensors outside tract boundaries is not represented in the ellipsoidal view of Figure A.4 for clarity. Setting the FA of points outside tracts to zero insured tract propagation would cease if tractography estimates strayed outside tract boundaries.

2.3.4 Simulating tract crossings

This thesis compared the performance of streamline tractography and front propagation tractography in the case of a simulated fiber crossing between two linear tracts of the form shown in Figure A.4 (a). Fiber crossings were simulated by defining two linear paths of diffusion tensors with strong orientational maxima in each respective tract direction. The area of intersection between each linear tract was assigned planar diffusion tensors based on the hypothesis that regions of intravoxel orientational heterogeniety give rise to oblate diffusion tensors [35]. Oblate tensors were defined with eigenvalue weights $\lambda_2 = \lambda_1 - 10^{-6}$ and $\lambda_3 = \lambda_1/10$. This eigenvalue weighting created tensors in which the direction of diffusion was ambiguous within the plane defined by the eigenvectors $\hat{v}_1$ and $\hat{v}_2$. An ellipsoidal view of the fiber crossing simulation described in this paragraph is shown in Figure A.5

As can be seen in Figure 2.6, the tensor field in oblate regions of tensor crossings was defined with an erroneous orientation halfway between each of the incoming tracts. Because planar diffusion tensors represent a breakdown in Gaussian form assumed in the Stejskal-Tanner equation [35], there is no reason to assume that the principal eigenvector of an oblate diffusion tensor approximates an orientation of underlying white matter structure. Therefore, in regions of planar diffusion tensors, the term principal eigenvector is slightly misleading, as $\hat{v}_1$ and $\hat{v}_2$ are weighted with
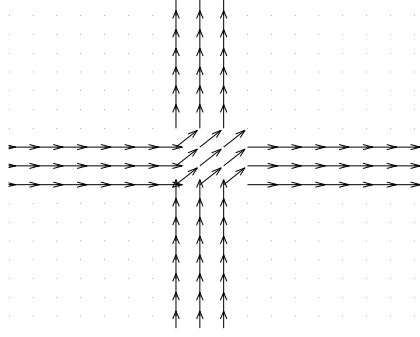
Figure 2.6: Principal eigenvector field for synthetic tract crossing with 90 deg angle of intersection. Oblate diffusion tensors in region of tract intersection are assigned principal eigenvector direction half way between tract orientations.

nearly identical eigenvalues, defining a plane. However, because streamline methods are based solely on following the principal eigenvector, it was important to define v_1 fairly so as to not bias comparisons of SLT and FPT performance. A principal eigenvector direction halfway between each incoming tract was adopted in the interest of allowing SLT estimates a chance to navigate tract crossings without exiting the $FA > 0$ boundary of the entire crossing structure.

2.3.5 Perturbing a diffusion tensor field

The diffusion weighted measurements used to construct the diffusion tensor contain thermal noise due to the random molecular motion of air within the scanner and RF noise due to the presence of electrical devices near the scanning area. Assuming the individual diffusion weighted measurements S_i used in the Stejskal-Tanner relationship of Equation 1.6 are random variables of a known distribution, it is possible to solve for the underlying statistical distribution of resulting diffusion tensor elements in closed form if statistical independence is assumed in the set of diffusion weighted measurements at a particular (x,y,z) voxel location. Accepting the premise of statistical independence, three random variable transformations would be required to solve

the Stejskal-Tanner system for diffusion tensor element random variable: division, natural logarithm, and addition. In reality, diffusion weighted measurements in a given voxel location are not statistically independent, since neighboring directional measurements certainly have related mean values. A closed form solution for the statistical distribution of diffusion tensor elements was not investigated further due to the statistical dependence of diffusion weighted measurements.

Because the focus of this research is a study of tractography algorithm performance, the central point of interest was how noise in DWI measurements effects tract estimation. A diffusion tensor has two descriptive properties: anisotropy and orientation. Noise in diffusion weighted measurements gives rise to changes in both the anisotropy and orientation of each diffusion tensor within a diffusion tensor field. These changes in diffusion tensor anisotropy and orientation give rise to angular deviations and tract termination conditions in DTI tractography estimates. This thesis explored the impact of noise in diffusion tensor fields by adding random perturbations to synthetic tracts that altered both the anisotropy and orientation of the simulated diffusion tensor fields.

In this study, perturbations were added to the synthetic diffusion tensor fields described in Sections 2.3.3 and 2.3.4 by adding a zero mean Gaussian random value to each of the six unique elements of the diffusion tensor. In general, any random perturbations would have provided the desired changes in diffusion tensor anisotropy and orientation. Gaussian perturbations were chosen for the sake of mathematical simplicity.

The standard deviation of the additive Gaussian perturbation was varied for purposes of studying the effects of greater amounts of diffusion tensor perturbation on tractography error. In each element D_i of each diffusion tensor in the $\mathbf{D}$ field, the standard deviation of the Gaussian perturbation was defined as a weighted ratio of the diffusion tensor element being perturbed. An equation describing the process used to weight the standard deviation of additive Gaussian perturbation appears as

Equation 2.18,

$$\sigma_i = w \cdot D_i, 1 \le i \le 6 \ , \tag{2.18}$$

where w is the weighting metric used to vary the amount of perturbation in each tensor element. The w perturbation weight has no physical interpretation and was simply used to compare tractography performance as a function of relative diffusion tensor perturbation.

This thesis explored the ability of both streamline and front propagation tractography algorithms to resolve known synthetic tract structures in the presence of noise perturbations in the diffusion tensor field. Trial studies were conducted in which both the streamline and front propagation algorithms attempted to traverse a noisy helical tract of weight w over the course of multiple random Gaussian perturbation trials. In each trial, each algorithm was assigned a pass or fail value based on whether a complete traversal of the helical tract was completed. A success probability was then defined as the number of successes in traversing a given synthetic tract divided by the total number of trial attempts. Success probabilities were calculated using data collected from 50 Gaussian perturbation trials at each noise weight. The binary success/failure nature of perturbation trial results yielded discrete measurements of an underlying Binomial distribution. The DeMoivre-Laplace theorem states that for a sufficiently large sample set n, a Binomial distribution with a probability success, p, and probability of failure, $1 - p$, may be approximated by a continuous Gaussian distribution $N(\mu, \sigma^2)$ of mean np and variance npq. [26].

$$\frac{n!}{(n-k)!k!}p^k q^{n-k} \approx N(np, npq) \tag{2.19}$$

The 50 repetition trial size used in this research provided consistent results when compared with slightly lesser trial sizes, and was therefore deemed acceptably large for use with Equation 2.19. Equation 2.19 was used in chapter three to report synthetic data perturbation results in terms of an observed normalized mean success rate p and a normalized standard deviation error-bar size pq.

In the interest of making trials unbiased, each algorithm was seeded to provide the best chance of detecting the helical tract. Thus, each trial represented error/success rates to the best ability of each algorithm. For each trial, the streamline algorithm was seeded on a whole pixel basis over the entire cross sectional diameter of the first axial slice of the helical tract. If a complete traversal was accomplished for any of the seed points from the first slice plane, the current trial was assigned a pass value. Front propagation of the FPT algorithm was seeded in the exact same manner as in the streamline algorithm. A greedy search from every point in the cross sectional diameter of the last axial slice of the helical tract was attempted for each seed point. If the FPT algorithm was able to completely traverse the helix from any end point to any seed point, the current trial was assigned a pass value.

2.4   Constructing a physical DTI phantom

A physical phantom was constructed in the interest of comparing tractography results to a ground truth model scanned in a clinical DTI environment. The tissue phantom was constructed using microbore PTFE tubing with dimensions: 0.305 mm ID, 0.702 mm OD. The micro-capillary tubing was cut into 10 mm lengths and positioned parallel to one another. Ten micro-capillaries were used in each sheet. The micro-capillaries were secured into sheets using packing tape. The micro-capillaries were then each filled with water using a 32 gauage micro-syringe. Once sheets of water filled micro-capillaries were built, the sheets were stacked in alternating perpendicular orientations and secured to one another using a thin amount of superglue. Because the PTFE tubing came in a spool, each micro-capillary retained memory of the spool curvature that could not be corrected. As such, a reasonably consistent amount of curvature was present in each of the micro-capillary sheets used to construct the tissue phantom.

A housing was constructed for the crossing microtubing structure using a thin plastic container and gelatin. Gelatin was used to remove air from the volume sur-

rounding the micro-capillary sheets, thereby reducing susceptibility artifacts. The plastic container/gelatin housing was created by poring an initial layer of gelatin and allowing it to set. The micro-capillary structure was then placed on top of the gelatin base. A second layer of gelatin was then pored into the container, creating an air free housing which surrounded the micro-capillary structure.

Figure 2.7: Photograph of components of attempted physical DTI phantom. Crossing structure is composed of sheets of 10 micro-capillary tubes of dimension: 0.305 mm ID, 0.762 mm OD. Five tubing sheets were stacked in alternating perpendicular orientations. Crossing was immersed in gelatin to reduce susceptibility artifacts. Phantom was housed in a thin plastic container. Quarter is shown to provide scale information.

Chapter 3

Results and Conclusions

This chapter presents results from a variety of experiments in which the performance of streamline tractography is compared to that of front propagation tractography. Tractography algorithm performance was compared using both software phantom data and real human brain data. Because of the existence of a ground truth in software phantom experiments, quantitative comparisons are presented between streamline and fast marching tractography algorithms. To the best knowledge of the author, this thesis is the first tractography research to quantitatively compare fast marching and streamline tractography algorithms using a software phantom ground truth.

Human brain data was also used to qualitatively compare SLT and FPT tractography performance. In human brain data, there is no ground truth with which to compare the output of tractography performance. DT-MRI tractography literature traditionally compares algorithm performance on a qualitative basis based on graphical comparisons of connectivity in output tractography visualizations. The highly oriented highly anisotropic region of the corpus callosum will be the focus of human brain tractography analysis. Because the author does not have a sufficient background in neural physiology to make comparative neural connectivity arguments, algorithm performance will be judged according to general agreement with corpus callosum visualizations found in DTI tractography literature.

A final section of results is presented for the physical DTI phantom constructed and scanned in this research. The results obtained from the physical phantom allow for a ground truth discussion of issues in DTI image resolution including signal to

noise ratio and spatial resolution. The effects of IVOH as reflected by planar FA images are also presented.

3.1   Software phantom results

3.1.1   Verification

The first study conducted in this research was a verification experiment in which each tractography algorithm operated on unperturbed, highly anisotropic, linear and helical tracts. Software phantom verification was an ideal means of tractography algorithm testing, since the ground truth of the input data was known down to the level of the diffusion tenor field. Output plots of helical and linear tracts for both algorithms are shown in Figure 3.1. Both algorithms provided accurate connectivity estimates in synthetic linear and helical tracts, supporting the ability of each algorithm to traverse both linear and curved tracts in three dimensions.

In Figure 3.1, front propagation tract estimates appear to be rougher than corresponding streamline tract estimates. This apparent roughness in FPT tractography estimates is due primarily to the usage of discrete voxel by voxel network approach used to draw connectivity estimates in the FPT algorithm. In both streamline and front propagation tract estimates, a linear point to point connection was used to visualize the connectivity described by the output tract point sets. Because the streamline algorithm traverses an interpolated three dimensional space in fractional voxel steps, the linear point to point visualizations of streamline tracts appear smoother. Additional roughness in FPT tracts results from speed biasing in directions of outward propagation connectivity, as noted in Chapter 2, Section 2.2.1. The discrete voxelized output FPT tracts could be visualized with greater smoothness through the usage of spline curve fitting. Further smoothness in FPT tract estimates could be realized through an increased neighborhood of connectivity during outward propagation. Because the purpose of this research was to explore the performance of tractography
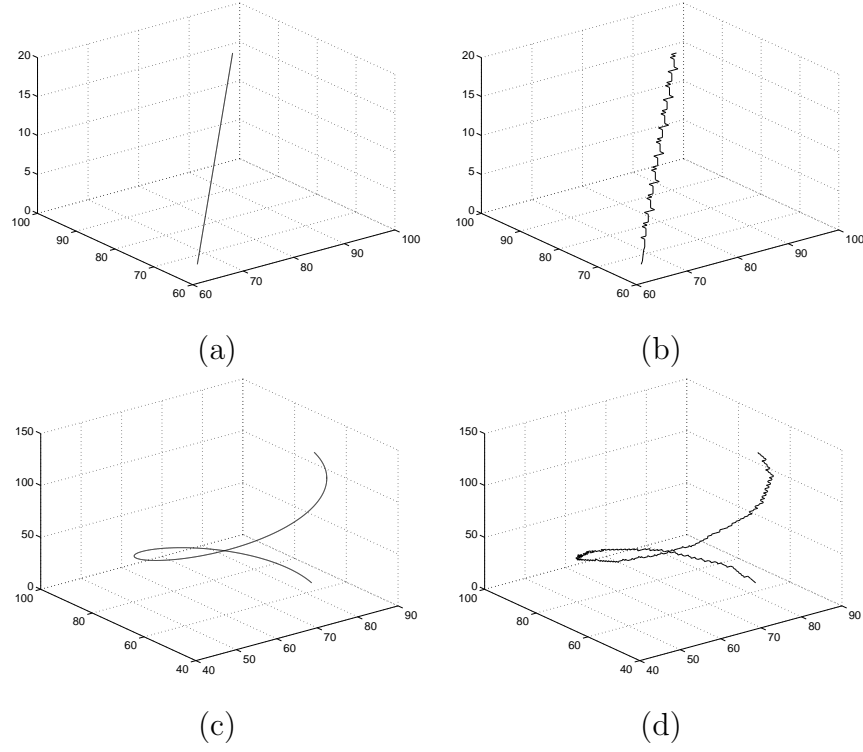
Figure 3.1: Verification of tractography algorithms using unperturbed software phantom tracts. (a) Streamline, linear tract (b) Front propagation, linear tract. (c) Streamline, helical tract. (d) Front propagation, helical tract. Streamline method tracts appear smoother than FPT tracts because streamline tract points are based on defined within an interpolated continuous space, and front propagation tract points are defined discretely.

algorithms in generating accurate connectivity estimates, and not to perform three dimensional visualizations, the roughness FPT tract estimates was deemed acceptable.

3.1.2 Diffusion tensor perturbations in single tract software phantoms

A comparative study was conducted on the ability of streamline and front propagation tractography algorithms to traverse noisy diffusion tensor fields in the case of single tract software phantoms. The impact of diffusion tensor perturbations arising from the presence of noise during diffusion weighted measurements was investigated using the perturbed synthetic helical tracts described in Chapter 2, Section 2.3. A helical tract was defined within an isotropically sampled synthetic data set with a 128 x 128 x 128 acquisition matrix. The helical tract was defined as a tube with an axial cross sectional diameter of four voxel widths. Each algorithm was seeded to provide the best chance of traversing the entire helix structure. For both algorithms, seed points were selected from every whole voxel included within the boundary of the first axial slice of the helical tract. Subvoxel seed locations were not explored in the streamline algorithm in the interest of reducing computation time and providing a consistent reference of comparison with the front propagation algorithm. End points were selected for the front propagation algorithm from the set of all whole voxel locations inside the last axial slice of the helical phantom tract. Each perturbation trial was deemed a success or failure based on whether or not a complete path of connection could be obtained between any of the seed point pixels in the bottom of the helical structure and the end point pixels in the top of the helical structure. The backward search capability of the front propagation algorithm allowed for a much greater number of connectivity investigations than the streamline algorithm in each trial. Given a set of M seed points and N potential end points, the front propagation algorithm explored MN per trial compared to the N connectivities explored by the streamline algorithm. Figure 3.2 provides tract estimation probability plots for streamline and front propagation tractography algorithms for varying levels of perturbation in the diffusion tensor $\mathbf{D}$.

Figure 3.2 exhibits the expected behavior of steadily decreasing tract estimation
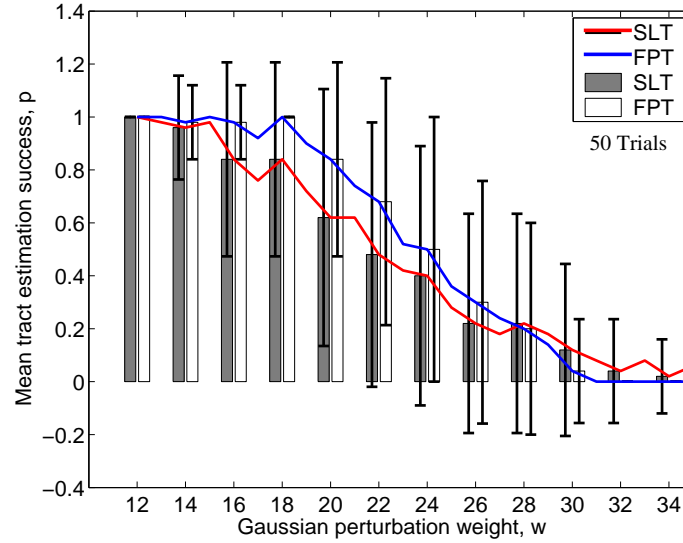
Figure 3.2: Bar plot comparing single tract performance in streamline and front propagation algorithms. As expected, both algorithms have increasingly poor success probabilities as perturbations in diffusion tensor field lead to erroneous angular deviations and propagation stoppage. The error bars indicate one standard deviation from the observed mean success rate, p. Within the error bar thresholds, there is no statistically significant difference in streamline performance vs. front propagation performance in the case of single tract software phantoms.

accuracy with increasing levels of diffusion tensor field perturbation. The included error bars indicate that there is not a statistically significant performance difference in either tractography algorithm for the perturbed single tract helix. This result of statistically equivalent connectivity accuracy is interesting given that the front propagation algorithm examined a greater number of potential connections than the streamline algorithm for each trial.

The single tract helical study provided insight into the way in which noise diffusion perturbations cause tract estimation failures in each algorithm. At sufficiently high levels of diffusion tensor perturbations, the FPT algorithm failed to provide tract estimates due to two reasons. In some cases, the windowed speed function was

not able to propagate in a sufficiently consistent direction, causing termination of forward propagation before the front could reach the top of the helix. In other cases, the monotonicity of the discretized time of arrival map was destroyed by the effect of perturbations during outward propagation, causing an inability of the greedy search to back-traverse the time of arrival map. Increases in diffusion tensor perturbation manipulated the interpolated eigensystem used by the streamline algorithms, causing maximum curvature and eigenvector sorting error flags to be set in the streamline algorithm. The observation of increasing maximum curvature detections and eigenvector error sorting detections with increasing levels of noise verified the usage of these propagation stoppage criteria as a means of limiting noise effects in tract estimates.

3.1.3   Phantom tract crossings

The effect of varying intersection angle and diffusion tensor perturbations on streamline and front propagation tractography algorithms was also explored. Analysis of tractography algorithm performance in the presence of crossings began with the study of unperturbed crossing fields with intersection angles of 30, 60 and 90 degrees. Seed points were selected from both intersecting tracts, and the same seed points were used in both SLT and FPT tract estimates. In front propagation estimates, potential endpoints were explored for symmetric regions in the regions of non-intersection that did not include seed points, insuring that tract estimates would traverse the region of intersection. Figure B.1 shows unperturbed tractography results from both algorithms.

In the streamline estimates of Figure B.1 (a) and (b), there are several features of interest. First, from any one seed point, the one to one connectivity of the streamline algorithm insures that a maximum of one branch of the crossing can be traversed. The branch selected by the streamline algorithm depends entirely on location of investigated seed points. In Figure B.1, streamline tracts follow the direction of the principal eigenvector in the region of intersection, even though the principal eigen-

vector is weighted only 10^{-6} higher than the second largest eigen-pair. Streamline tracts follow the principal eigenvector direction of the directionally ambiguous oblate diffusion tensor field until tract propagation steps within the neighborhood of one of the anisotropic, homogeneous tract branches. Within the intersection area, interpolation of the diffusion tensor field causes tract estimates to be steered in the direction of the nearest non-intersecting tract region. Viewing streamline propagation for the ninety degree case of Figure B.1 (b), two of the six chosen seed points do not traverse the crossing region. These halted tracts attempted to make large angular deviations due to the nearby presence of diffusion tensors of orthogonal orientation. The halted streamline tracts ceased propagation due to detection of an eigenvector sorting error, as the principal eigenvector direction changed dramatically between successive steps, causing the second largest eigenvector to be better aligned with the previous step direction. Had a curvature threshold less than approximately 90 degrees had been used, propagation would also have ceased due to excessive tract curvature. The ninety degree crossing case illustrates that eigenvector sorting conditions and curvature thresholds can limit the ability of streamline algorithms to propagate in regions of of tract crossings. Because the propagation constraints placed on streamline algorithms are motivated out of an anatomical constraint that white matter tract curvature should not deviate highly in successive sub-voxel steps, removing curvature constraints from the streamline algorithm in favor of allowing traversal of crossing regions would allow for erroneous, highly noise-influenced tract estimates.

Similarly, there are a number of interesting features in the FPT tract estimates of Figure B.1 (c)-(f). A first noteworthy feature of the FPT estimate of (c) is that the front propagation/backward search process of the FPT algorithm leads to a connection from each seed point to each of the three other regions of non-intersecting tract structure at the chosen likelihood threshold of 50%. The 50% likelihood threshold was selected arbitrarily to limit the number of visible tracts in the FPT estimates of Figure B.1. The ability of the FPT algorithm to describe the entire crossing structure

from each of the three seed points is a significant performance benefit over streamline tract estimates in regions of crossings.

A second feature of note is that the proposed FPT algorithm proposed is biased toward selecting tracts of low curvature in the case of intersecting tracts. This bias stems from the use of alignment of future points in the normal direction from the interface with past band tensor orientations in the speed function of Equation 2.5. In the highly anisotropic, completely homogeneous phantom tracts of Figure B.1, at the point where the interface enters the crossing, all past band diffusion tensor orientations point in the direction of the tract from which propagation started. The use of past band diffusion tensor orientations to govern speed of propagation to figure points gives rise to a concept of propagation memory, or momentum, in the outward propagating front. Once the interface begins to move with relatively high speed in a homogeneous direction, propagation continues in that direction even if the interface is slowed and widened in regions of intersection. In plots (c)-(e), the highest tract density consistently appears in the opposing tract branch oriented along the linear direction from which forward propagation was seeded. At the chosen likelihood threshold, the low curvature bias in tract estimates provided by the FPT algorithm caused no tract estimates to be drawn in (d) between the chosen seed points and the bottom branch, since propagation into the bottom branch required the greatest curvature. In the 90 deg crossing case of (e) and (f), the FPT algorithm was able to accurately estimate connectivity without the curvature thresholding problems encountered by the streamline algorithm in cases of large intersection angles.

Based on the low curvature tract selection biasing noted in the unbiased linear crossing FPT experiment, a separate experiment was conducted to study whether or not there was a minimum intersection angle θ below which a complete linear crossing structure could not be completely resolved. In the case of a crossing structure of intersection angle θ, the limiting case of completely resolvable structure occurs when a tract is seeded inside a homogeneously oriented single tract branch of the crossing

and the front propagation algorithm attempts to back-traverse from the tract region oriented at $180 - \theta$ degrees to the original seed region. Figure B.2 shows speed of arrival maps for intersection angles of 35 deg and 36 deg.

In the case of the 35 degree intersecting structure, the interface did not propagate into the tract oriented at 145 deg to the seeded tract. Looking at the speed of arrival intensity, it can be noted that the front interface did slow down and spread out as it reached the region of intersection. However, the front did not propagate the region oriented at 145 degrees due to the windowing of the speed function and the high required curvature of interface propagation relative to the initial seed location. For the 35 degree intersection of Figure B.2, potential tracts are overlaid over the speed of arrival image in blue. Because the forward propagating front did not arrive at the branch oriented at 145 degrees, tract reconstruction is not possible. A similar plot is shown for a linear tract intersection of 36 degrees in Figure B.2 (b). In this case, the front was able to forward propagate into the branch oriented at 144 degrees to the seed tract location, allowing for backward reconstruction of the entire crossing structure from the initial seed location.

While the completely homogeneous regions of non-intersection and the oblate tensor definitions used in this software phantom experiment are an idealized situation, this experiment demonstrates that windowing the angular band of allowed propagation in the speed function creates a minimum angle of tract intersection below which crossings cannot be fully resolved from a single seed point. The speed function proposed in Equation 2.5 trades a loss in resolvable structure for computational efficiency and more meaningful likelihood estimates. Windowing of the speed function is more computationally efficient because it does not give rise to heap insertions and removals to points to which there is little probability of connectivity described by the local diffusion tensor field. The likelihood estimates that result from the use of the speed function of 2.5 are said to be more meaningful because points that lie in low probability directions of anisotropic diffusion from a past band point $\mathbf{r}$ are not assigned time of

arrival values, and therefore effectively receive zero likelihood of connection to point **r**. Because the speed function of 2.5 limits the allowed range of propagation based on the probability defined by the ODF, an unavoidable result is a loss in connectivity to certain regions, including crossings below a minimum angle of intersection. It is true that the speed function proposed in [35] allows for complete resolution of tract crossings at any angle of intersection, due to the lack of limits imposed on allowed front propagation directions. However, the speed function of [35] listed as Equation 1.20 depends on the concept of a principal eigenvector field, which has no meaning in the regions of planar diffusion tensors encountered in tract crossings.

The next stage of comparison of streamline and front propagation based tractography algorithms consisted of an investigation of behavior in the case of noise perturbed linear tract crossings. Figure B.3 provides an example of tractography performance in the presence of slight perturbations of the diffusion tensor field in which zero mean Gaussians of $\sigma = 0.005D_i$ were added to each diffusion tensor element in the crossing field. In (a) and (b), a number of halted tracts may be noted in the center region of the tract crossing. All of these halted tracts stopped in the center tract region due to the detection of an eigenvector sorting error due to noise perturbations changing the principal eigenvector orientation dramatically in successive steps. Because of the highly planar nature of the simulated planar tensors in the region of intersection, where $\lambda_1 = \lambda_2 + 10^6$, the streamline algorithm was extremely prone to forward propagation failure due to curvature and eigenvector biasing criteria. The points seeded from the lower right branch show the effects of interpolation within a noisy-oblate field, as both dashed tracts followed a different path through the crossing structure compared to the unperturbed case of Figure B.1.

Comparatively, the tract estimates of Figure B.3 (c)-(f) suggest that connectivity estimates provided by the front propagation algorithm are less effected by noise perturbations than streamline estimates. The perturbed front propagation estimates of Figure B.3 all describe the same general connectivity as the unperturbed estimates

of Figure B.1. Figures (c), (e), and (f) appear nearly identical to the unperturbed case. Figure B.3 (d) describes a lower tract density in the linear direction compared with the unperturbed tract estimates of Figure B.1, however the general connectivity information in both plots remains the same.

A quantitative perturbation analysis similar to the noisy helix experiment described previously was also conducted on simulated crossing linear tracts. The effect of diffusion tensor perturbations in both algorithms was compared for synthetic linear tract crossings of 30, 60, and 90 degrees. A series of 50 trials was conducted for each perturbation level. For each streamline trial, the streamline algorithm was seeded from a clearly defined tract region in the direction of a crossing. Trials in which streamline propagation entered one of the three other non-intersecting regions of the crossing structure were counted as successes. Trials that did not reach the three opposing non-intersecting regions due to propagation outside the crossing structure, eigenvector sorting criteria, and curvature criteria were treated as failures. Trials for the front propagation algorithm were essentially conducted in reverse. Outward front propagation was seeded from the same location as streamline trials. One point in the center of each of the three opposing non-intersecting tract regions was selected as a potential end point from which to attempt greedy searches on the time of arrival map back to the seed point. If any of the three end points was able to find a greedy-cost path back to the seed point, the perturbation trial was counted as a success. Figure B.4 summarizes the results of the linear crossing perturbation trial experiment described in this paragraph.

Figure B.4 illustrates that the front propagation algorithm has a statistically meaningful performance advantage over streamline tractography in all of the intersection angles explored. For the 30 degree intersection case of (a),the front propagation algorithm was able to estimate at least one out of the three opposing tract connections to the chosen seed point with greater frequency than the streamline algorithm for zero mean Gaussian perturbations of up to $\sigma = 0.44 D_i$ for each tensor element in

the diffusion tensor field. Similarly, the FPT algorithm displayed a mean tract estimation success rate superior to that of SLT for Gaussian noise weights of up to 0.44 for 60 degree intersections, and noise weights of up to 0.46 for 90 degree intersections.

The superiority of the FPT algorithm in cases of tract intersections is due to two principal causes. First, the backward search capability of the front propagation algorithm allowed for the investigation of many more potential connections than the one to one forward connectivity of the streamline algorithm. Although the connectivity advantage of FPT over SLT was limited to 3:1 in this experiment to ease computation time, the FPT algorithm would likely have displayed a greater advantage over the SLT algorithm for higher diffusion tensor perturbation levels had greater numbers of greedy cost paths been explored in each trial. A second important advantage of the FPT algorithm is the forward propagation windowing provided by the ODF construction of the speed function of Equation 2.5. Because the ODF based speed function broadens propagation within regions of planar tensors rather than following the erroneous direction of the principal eigenvector field of $\mathbf{D}$, backward searches on the time of arrival map built by the time of arrival map allow for more accurate descriptions of connectivity between two branching or crossing regions. The high failure rates noted in the SLT algorithm were a result of the general instability of the eigensystem of oblate diffusion tensor regions in the presence of noise perturbations. Because the FPT speed function does not rely on diagonalization of the diffusion tensor, resulting time of arrival maps are less effected by slight perturbations in diffusion tensor geometry, leading to more accurate tract estimates in cases of perturbed diffusion tensor fields.

3.2   Human brain results

Human brain data was also explored for qualitative comparison with results presented in other DTI tractography literature. The human brain data set studied was taken from the public domain DWI data set included with the SCIRun/BioPSE software

package developed by the Scientific Computing and Imaging Institute at the University of Utah [19]. The DWI data set was obtained using the 3 Tesla GE Signa scanner at the Laboratory for Functional Brain Imaging and Behavior at the University of Wisconsin, Madison. The DWI data set was imaged at 1.5mm isotropic voxel resolution using an EPI sequence with 12 non-collinear DWI measurements and 1 non-diffusion weighted measurement per voxel. Eddy-current distortion correction was not applied to the DWI images prior to tract estimation.

The highly organized, large bundles of white matter in the corpus callosum of the human brain have been used in DTI literature as a qualitative benchmark for tractography algorithm performance [2] [11] [27]. The anatomical structure of the corpus callosum is well known due to dissection studies in human cadavers [33] and experimental surgeries in living epileptic patients [22]. The corpus callosum is a large U shaped fiber bundle located in the lower mid-portion of the cerebrum and serves as the main bridge of white matter connection between the left and right hemispheres of the brain [33]. There are three main regions of the corpus callosum as seen from a sagittal cross section: the splenium, genu, and the body. A sagittal FA cross section taken between the left/right hemispherical midline is included as Figure B.5. The splenium and genu are the downward curving portions of the corpus callosum oriented posteriorly and anteriorly, respectively. The body of the corpus callosum the large horizontal region between the splenium and the genu.

Seed points for tractography estimation were selected from visual inspection of the FA images of Figure B.5. Looking at the coronal/axial slice plane view, the general structure of white matter connections between the cerebrum and the corpus callosum may be visually inferred, allowing for a selection of appropriate regions of seed points. Regions of seed points were selected manually by tracing the FA maps of B.7. Regions of potential tract end points were selected in the same manner for use in greedy path searches in the FPT algorithm.

A three-dimensional visualization of the diffusion tensor ellipsoids of the corpus

callosum is provided in Figure B.6. Figure B.6 illustrates the high orientational homogeneity of diffusion tensors in the region of the corpus callosum. The low transparency of the ellipsoids in the visualization indicates strong anisotropy in local water diffusion. The general shape of tract estimates that should result from the corpus callosum area apparent in this ellipsoidal view, with lateral connections moving between the left and right hemispheres leading to vertical connections moving upward into the cerebrum.

A streamline estimate of the corpus callosum structure appears as Figure B.7. Streamline corpus callosum tract estimates were obtained using a minimum FA criteria of 0.42, a maximum successive step curvature of 90 degrees, and a Euler's method step size of 0.1 voxel widths. In Figure B.7, output streamline tract estimates are shown in a three dimensional visualization with a bottom axial FA slice plane provided for visual orientation. The corpus callosum structure shown in Figure B.7 is consistent with the structure seen in streamline corpus callosum visualizations presented in [2]. As expected, large groups of coherently oriented U shaped bundles arch into the more upper regions of the cerebrum. The general geometry of the U shaped tracts agrees with the general geometry described in the coronal FA image of Figure B.5 (c). A general symmetry of connections between the left and right hemispheres of the brain can be noted. The largest density of tract estimates terminated between 7 to 12 slices above the body of the corpus callosum, traversing a vertical distance of between 10.5 mm to about 18 mm. Some connections extended much further into the extreme upper regions of the cerebrum. A few relatively randomly oriented outlying tract structures were also be noted in the included streamline visualization, most notably a tract estimate moving vertically from the center of the body of the corpus callosum. Such outlying tract estimates may have been removed had more strict propagation criteria been used. However, because there is no quantitative means of selecting FA propagation thresholds, adjusting streamline criteria to reduce or increase tracts of a certain structure is a rather arbitrary process.

A front propagation estimate of the corpus callosum for three different likelihood thresholds is shown in Figure B.8. Highest Nth percentage likelihood thresholds of 75, 50, and 25 percent were used in visualizations (a)-(c), respectively. Potential end points for greedy-cost path searches were defined in the highest axial plane reached by streamline corpus callosum tract estimation, corresponding to a physical distance of approximately 30 mm above the base of the corpus callosum. The front propagation estimates generally describe the same connectivity as the streamline method, with U shaped connections about the sulci between the left and right hemispheres. As expected, the density of visible tract estimates is reduced as the Nth percent likelihood threshold is increased. An interesting feature of Figure B.8 is that at all of the likelihood thresholds explored, the highest density of connections corresponds to seed locations around the splenium of the corpus callosum. This result indicates greatest confidence in tracts around the splenium, suggesting higher combined homogeneity and anisotropy of diffusion.

Figure B.9 allows for visual comparison between the corpus callosum tract estimates provided by each algorithm, with the most likely 50% of FPT estimates shown in red, and the streamline estimate of Figure B.7 shown in blue. Figure B.9 illustrates that there is little difference between the connectivity described by each algorithm in the case of the well organized white matter structure between the cerebrum and the corpus callosum. A feature of note is that the longest tracts estimated by the streamline function occur in the region of the splenium, indicating a correspondence between tract length in streamline estimates and tract likelihood as defined in the FPT algorithm. Because the FPT algorithm embeds a combined notion of anisotropy and homogeneity in terms of speeds of arrival, it follows that tracts of highest speed should correspond to regions for which the validity of the streamline approximation to tract orientation is the greatest. The likelihood estimate defined in Equation 2.9 is defined in terms of average propagation speed, and therefore it is not surprising that tracts for which the streamline estimate are most accurate generally to longer

streamline tracts, and more likely front propagation tracts.

As was the case in the synthetic data study, the sub-voxel interpolated tract esti-mates of the streamline algorithm provide smoother visualizations of the underlying tract structure, however both algorithms depict the same anatomical structure. The agreement between streamline and front propagation estimates in the region of the corpus callosum is not surprising. The principal eigenvector field used by the stream-line algorithm in the region of the corpus callosum is a valid approximation to local fiber orientations since the required conditions of high anisotropy and high organiza-tion are met in the tract connections between the corpus callosum and the cerebrum. Had regions of lesser orientational homogeneity and anisotropy been explored, the streamline algorithm and front propagation algorithm would describe different con-nectivities. Such human brain regions were not explored, due to the lack of a ground truth by which to weight the different tract estimates provided by each algorithm.

3.3   Physical phantom results

The physical phantom constructed in this project was scanned using a 1.5T GE Signa scanner at Wake Forest University Baptist Medical Center. DWI data was acquired using an echo-planar imaging sequence with a spatial resolution of 2mm x 2mm in plane, and 4mm out of plane. For each voxel, 25 diffusion weighted images were obtained using isotropic angular sampling. A non-diffusion weighted T-2 image was also acquired at each voxel location. The 90 degree crossing phantom was positioned into the scanner such that one of the sets of crossing micro-capillary sheets was oriented out of plane, and one of the sets of micro-capillary sheets was oriented in plane. Figure B.10 (a) shows an axial FA slice in which two of the micro-capillary sheets are completely visible in plane, and the other 3 stacked sheets are visible coming orthogonally out of the slice plane. The high FA intensity of the water filled micro-capillary sheets of (a) relative to the background intensity indicates the presence of anisotropic water diffusion within the tubing structures. Another notable feature of

the included FA axial image is that within the region of perpendicular tract crossing, the orientation of the in plane tubing sheets can no longer be visually inferred due to insufficient spatial resolution. Within the tightly packed region of the tubing crossing, there was a separation of approximately 0.46mm between the overlapping tubing structures. Thus, the FA signal from up to four different tubes of orthogonal orientations may be present within the same voxel sample, giving rise to partial volume effects and a general loss of validity in the diffusion tensor model as a result of intra-voxel orientational heterogeneity.

Although the crossing tract structure may be inferred visually from the fractional anisotropy of diffusion tensors within the physical phantom, neither of the tractography algorithms explored were able to draw meaningful connectivity estimates within the phantom tracts. Figure B.10 (b) is a visualization of the diffusion tensor ellipsoids within the in plane structure of (a). The color coded diffusion tensor orientations illustrate that there is very little directional coherence in the diffusion tensors within the tubing structures, although the low transparency of the diffusion tensors indicates high amounts of anisotropic diffusion. Red colored ellipsoids best describe the expected diffusion tensor orientation of water restricted within the in plane tubing structure. Viewing (b), there is a noticeable lack of appropriately oriented diffusion tensors, and the diffusion tensors of highest anisotropy generally point in orthogonal directions to the restrictive boundaries of the in-plane phantom tracts. The combination of noticeably elevated fractional anisotropy values within the tubing structure and anisotropic, yet directionally incoherent diffusion tensors is probably due to an insufficient level of measured diffusion weighted signal in the voxelized DWI data used to construct DTI data. Because the in-plane structures visible in (a) only occupy roughly 1/6 of an in-plane voxel width, and 1/12 of an out of plane voxel width, there was very little restricted water present within any one voxel sample. It is likely that while the FA metric is sensitive to the presence of restricted diffusion within a voxel, greater amounts of diffusion weighted signal are required to accurately construct dif-

fusion tensors of accurate orientation.

3.4 Conclusion and discussion of further work

3.4.1 Conclusion

This thesis has presented a performance comparison of streamline and front propagation tractography methods against both ground truth and human brain DTI data. In comparing streamline and front propagation methods, two general themes emerged. First, both streamline methods and more complex front propagation techniques provide similar tract estimates when the underlying fiber structure in a region is orientationally homogeneous and sufficiently anisotropic. Perturbed single tract helical trial experiments suggest that if underlying white matter structure is structurally homogeneous on or above the scale of a voxel size, both streamline and fast marching methods will provide similar results given noise perturbed diffusion tensor data. Human brain corpus callosum results also illustrate the similarity of streamline and fast marching methods in the presence of large, homogeneous, anisotropic structure.

The speed function and likelihood estimates proposed for use within the general framework of the FMT algorithm developed by Parker [27] have been shown to provide tract estimates consistent with the known anatomy of the corpus callosum and with known geometry of ground truth software phantoms. The windowed ODF based speed function listed as Equation 2.5 was shown to allow for an estimation of complete linear crossing structures from a single seed point down to a minimum angle of intersection θ_t. While the windowing of the speed function creates a limit as to the range of resolvable tract intersections, the interface propagation defined by windowed propagation was shown to more accurately reflect the anisotropy and geometry of the local diffusion tensor field than propagation rules based upon diagonalization of the diffusion tensor. Because of the connection between propagation speed and likelihood estimates in front propagation algorithms, windowing the speed function assigns zero

likelihood connections between regions of low anisotropy and/or poor alignment with the local diffusion tensor field.

Software simulations containing fiber crossings clearly demonstrate the superiority of front propagation tractography over streamline methods in cases of IVOH. In unperturbed cases, it verified that the backward search of the time of arrival map allowed by the front propagation construct of FPT allows for 1 to N connectivity from a seed point, as opposed to the 1 to 1 connectivity assumed by forward propagating streamline methods. The instability of the eigensystem of the diffusion tensor field in cases of noise perturbed oblate tensor regions was reflected by the comparatively poor performance noted in streamline algorithm. The instability of noisy oblate diffusion tensor fields suggests that ODF based FPT speed functions have greater stability than speed functions based upon diagonalization.

Although the constructed physical phantom did not result in meaningful tractography estimates, a number of important trends in measured DTI data were noted. It was demonstrated that water filled micro-capillaries do provide a sufficiently small and restrictive boundary of diffusion to give rise to visually discernible structure in fractional anisotropy images. The concept of partial volume effects in DTI data was illustrated by the blending of tracts of multiple orientations into a single dark region on the axial FA map of Figure B.10.

3.4.2 Further work

The FPT algorithm proposes several variations of the FMT algorithm developed in [27], and therefore a performance comparison should be made between each algorithm. Component by component comparisons of the different speed function, connectivity methods, and likelihood estimates of the different front-based tractography algorithms are needed. Such a comparison was not attempted due to the disconnect between the discrete greedy connectivity method used in the FPT algorithm and the interpolated gradient descent method used in FMT. One common aspect of front-based tractog-

raphy algorithms to this point that requires improvement is the arbitrary nature of Nth percentile thresholding of tract estimates. The clinical application of likelihood estimates would benefit greatly from an automated means of selecting a pass and fail band of tracts described by front propagation algorithms.

Comparison of any two DTI tractography algorithms requires a gold standard of reference. The creation of phantom DTI tract systems on the scale and complexity of human neural anatomy is required before meaningful comparisons between different approaches to the tractography problem can be made. The materials and approach used in the phantom created in this research provided reasonable quality DTI images without notable susceptibility artifacts or distortions. The use of smaller microbore tubing bundled at the scale of a voxel sample would likely give rise to useful DTI phantom data sets. A specific phantom investigation should be made as to the impact of fiber crossings and branches on DTI tractography.

Appendix A

Illustrations of Methods

(a)

T=50
T=40
T=30
T=20
T=10

(b)
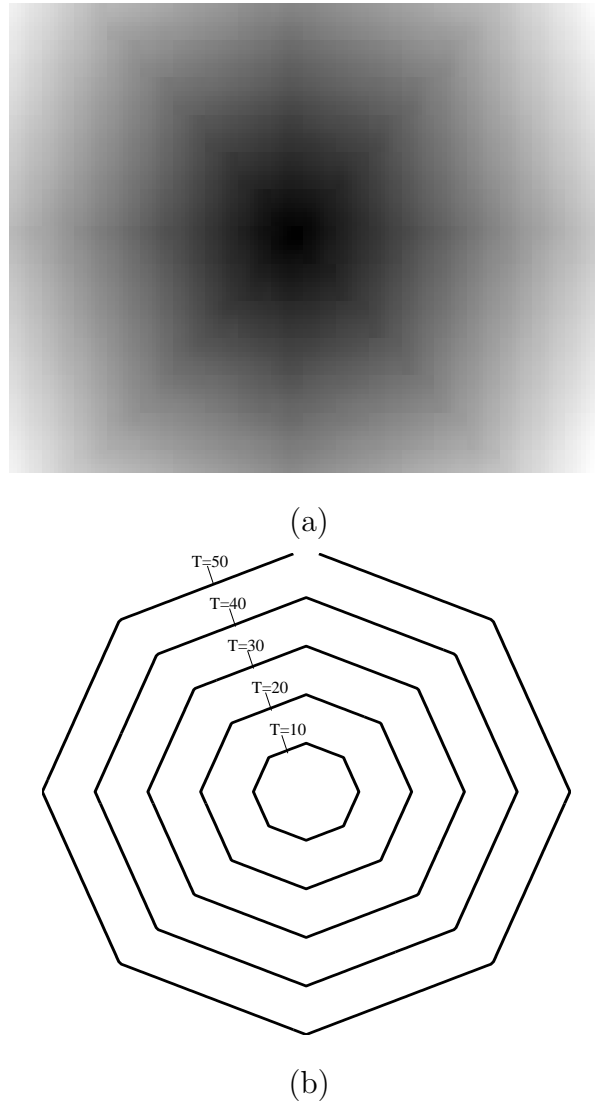
Figure A.1: Demonstration of outward propagation with constant speed function. Octagonal biasing of what should be spherical propagation is artifact of connectivity used to propagate the front. (a) Intensity image with brighter intensities corresponding to larger times (b) Isobars of propagation speed.
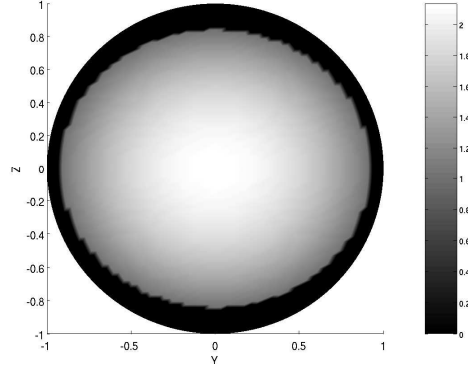
(a)
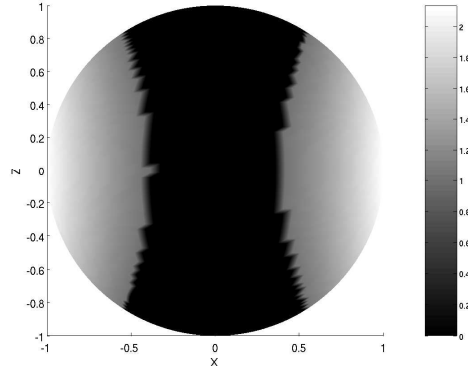
(b)
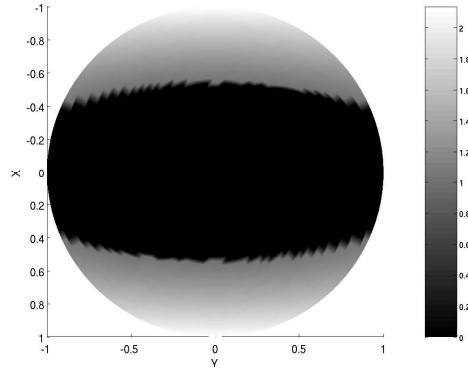
(c)

Figure A.2: $F(\hat{u})$ projected onto unit sphere. $\hat{v}_1$ oriented in $\hat{x}$ direction. $FA \approx 0.63$. Brighter intensity represents faster propagation speed $F(\hat{u})$ in a unit vector direction $\hat{u}$ from the origin of the unit sphere. Boundary between black and lighter intensities is boundary of allowed propagation directions $\hat{u}$. Propagation is fastest in direction of orientational maximum of diffusion tensor and is limited to a narrow band of directions and is limited to a relatively narrow band of directions due to high tensor anisotropy. (a) Y-Z View (b) X-Z View (c) X-Y View
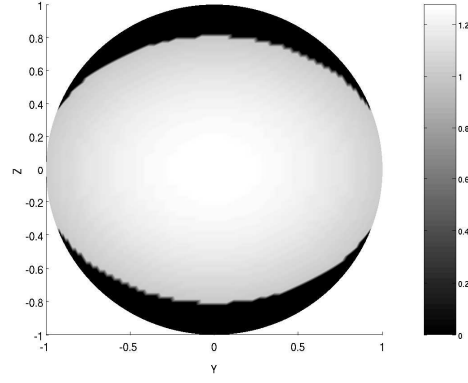
(a)
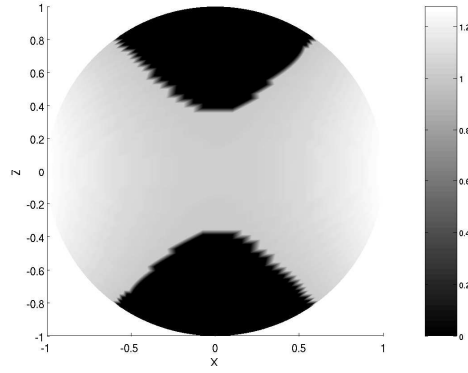
(b)
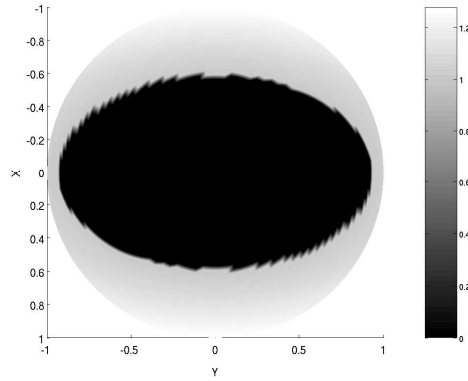
(c)

Figure A.3: $F(\hat{u})$ projected onto unit sphere. $\hat{v}_1$ oriented in X direction. $FA \approx 0.20$. Orientational maximum in $\hat{x}$ direction. In comparison to the ODF of Figure A.2, more isotropic ODF has broader range of propagation directions shown by non-black regions. Smaller, more uniform intensity values appear on surface, yielding similar propagation speeds in all allowed propagation directions $\hat{u}$. (a) Y-Z View (b) X-Z View (c) X-Y View
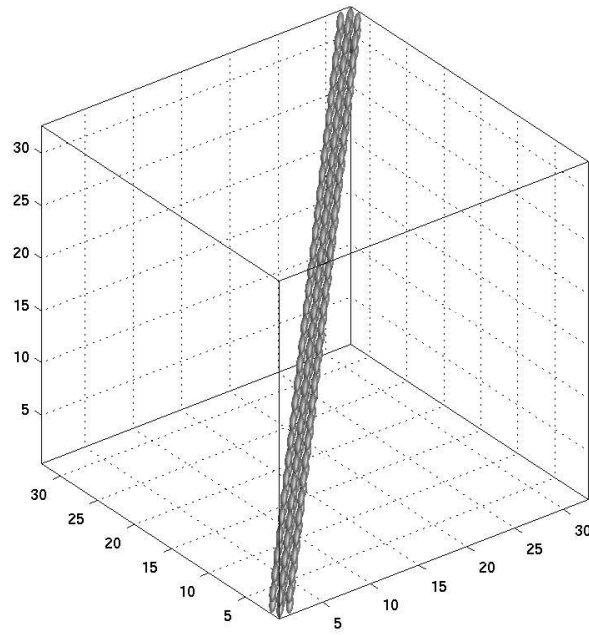
(a)
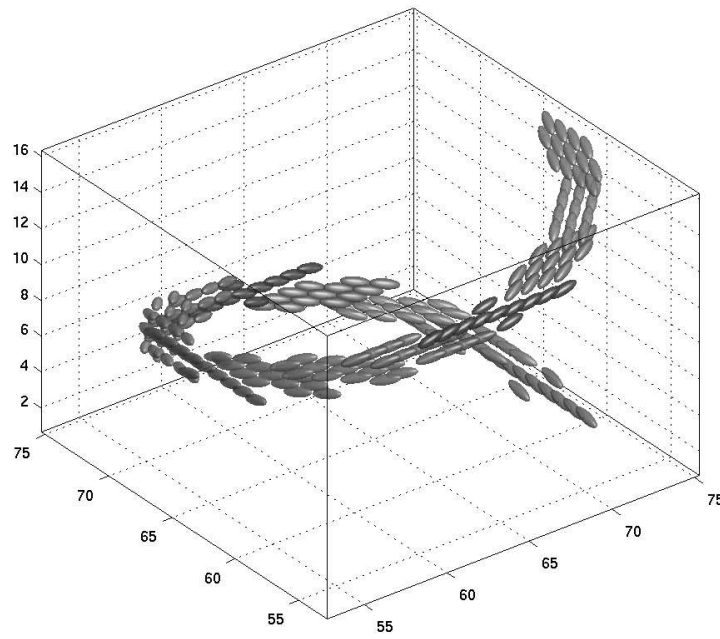
(b)

Figure A.4: View of diffusion tensor ellipsoids within software phantoms. Axes have no physical meaning and are provided simply for better 3-D perspective of structures. Color of ellipsoids reflects tensor orientation. Plots obtained using spm2 Diffusion toolbox. (a) Diffusion ellipsoids within linear tract. (b) Diffusison ellipsoids within single turn helical tract
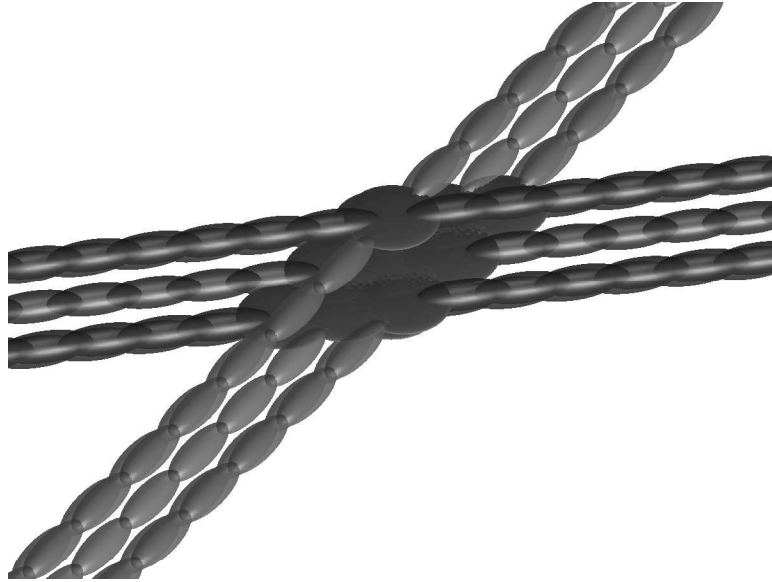
Figure A.5: Tensor field of tract crossing software phantom. Intersection angle is 45 degrees. Planar (oblate) tensors can be noted in region of tract intersection. Shading of ellipsoids reflects principal eigenvector orientation. In this figure, oblate tensors have principal eigenvector in direction of tract with matching ellipsoid shading.

Appendix B

Illustrations of Results
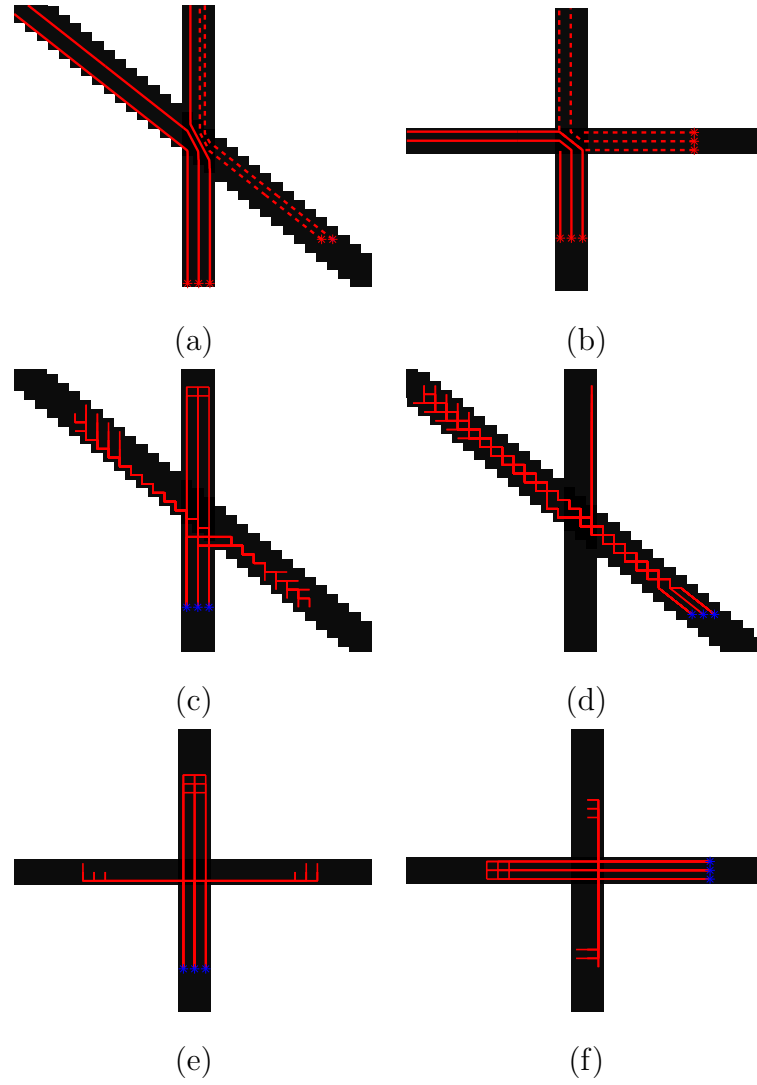
Figure B.1: Comparison of tract estimation in unperturbed, homogeneous crossing tensor fields. Seed points denoted by * symbols. Dashing on streamline tracts is provided to allow for visual separation between tracts seeded from different regions. (a) SLT, 45 deg crossing. (b) SLT, 90 deg crossing. (c) and (d) FPT, 45 deg crossing. (e) and (f) FPT, 90 deg crossing.

(a)

(b)
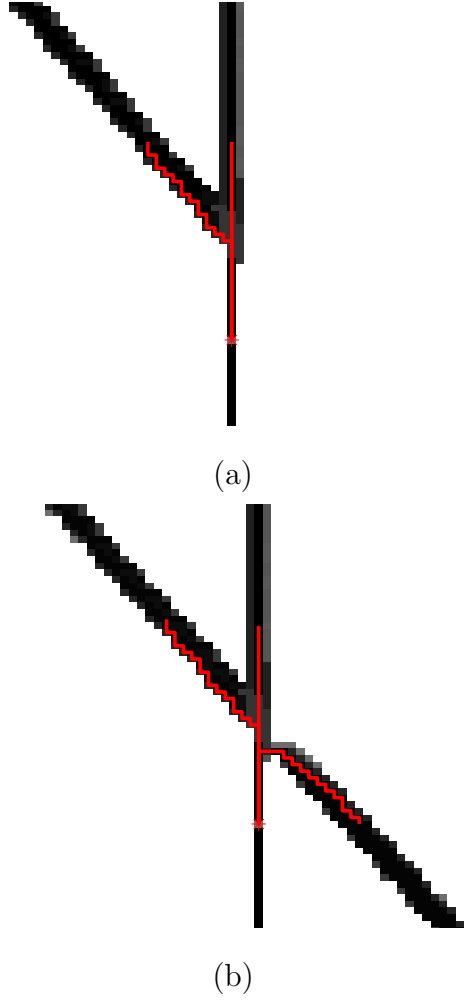
Figure B.2: Speed of arrival maps and resulting greedy cost paths from synthetic data crossing. Oblate tensors in area of tract intersection cause reduced propagation speed. There is some angular threshold θ_t below which tract oriented at $180 - \theta_t$ degrees to seeded tract is not explored during outward propagation, causing tract crossings to be incorrectly resolved as tract branchings. For the synthetic tracts and front propagation algorithm of this research, the limit of resolvable intersection angle, θ_t, was approximately 35 degrees. (a) 35 degree intersection (b) 36 degree intersection
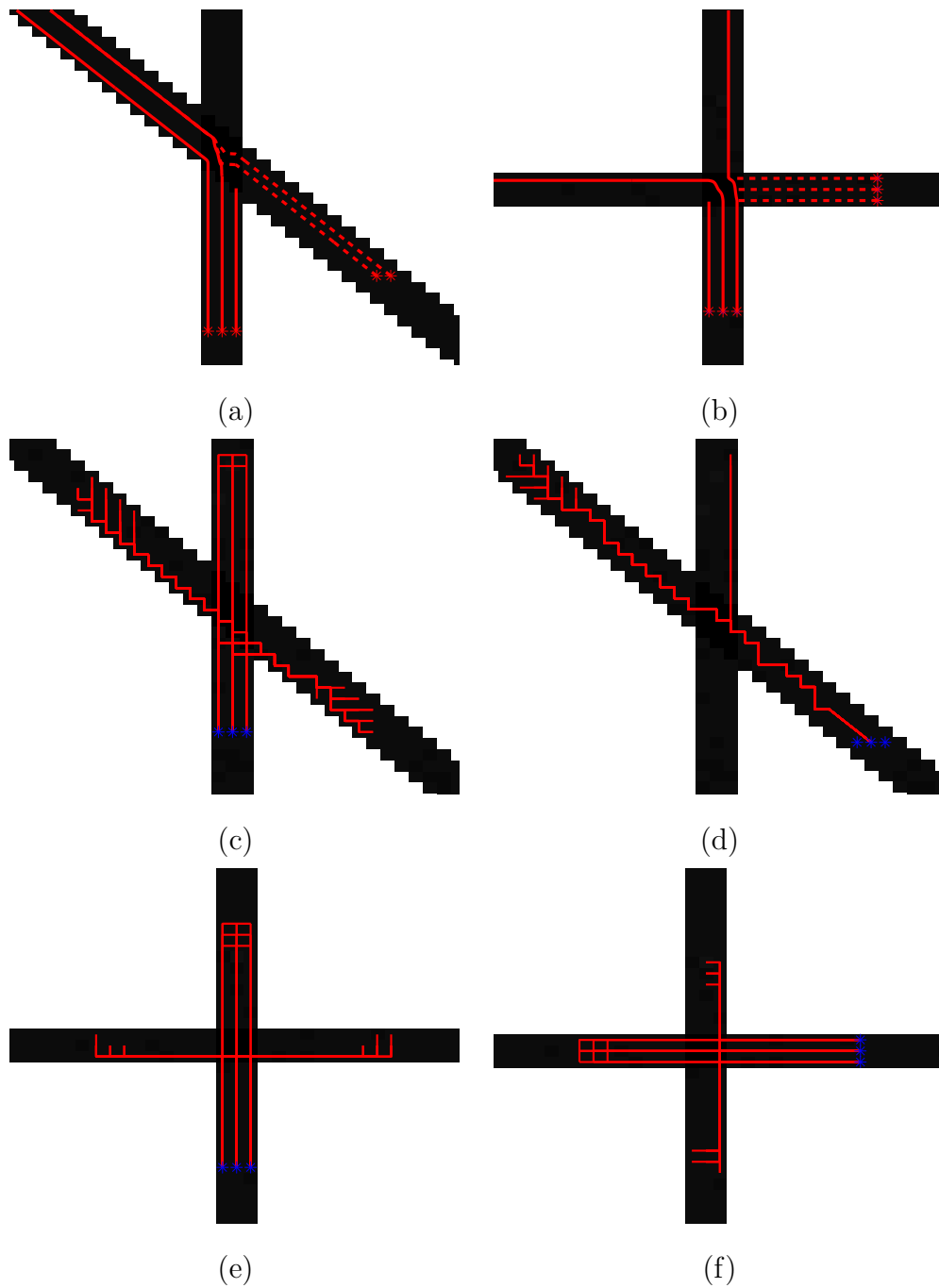
Figure B.3: Comparison of tract estimation in slightly perturbed crossing tensor fields. Gaussian perturbation of $\sigma=0.005D_i$ added to each tensor element of each diffusion tensor in field. (a) SLT, 45 deg crossing. (b) SLT, 90 deg crossing. (c) and (d) FPT, 45 deg crossing. (e) and (f) FPT, 90 deg crossing.
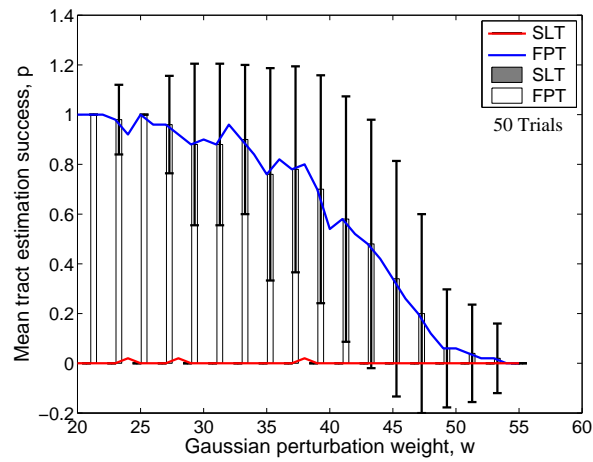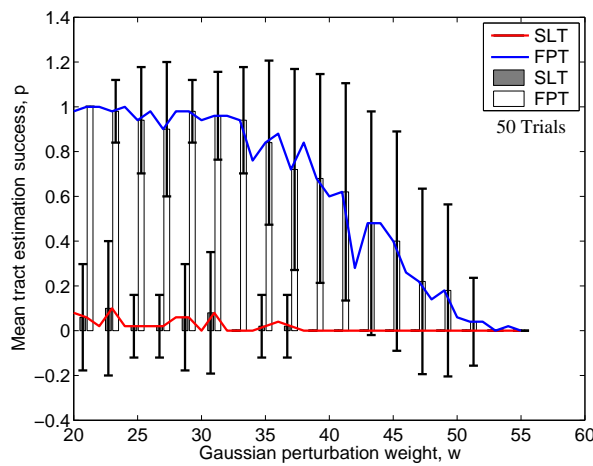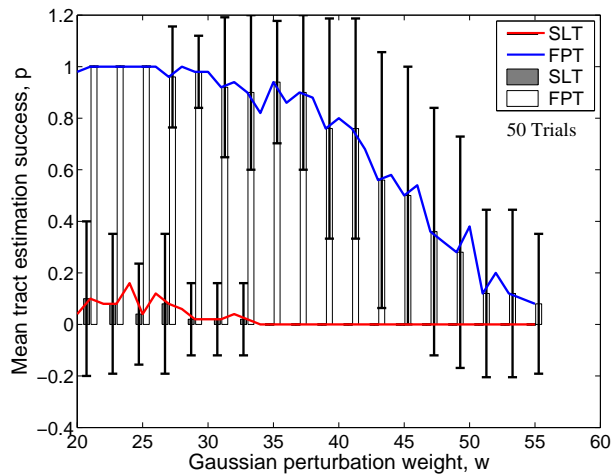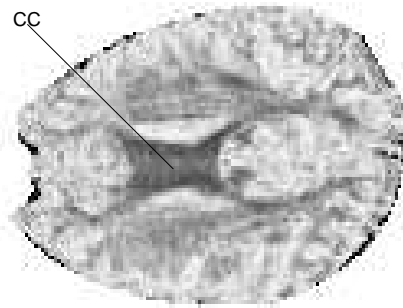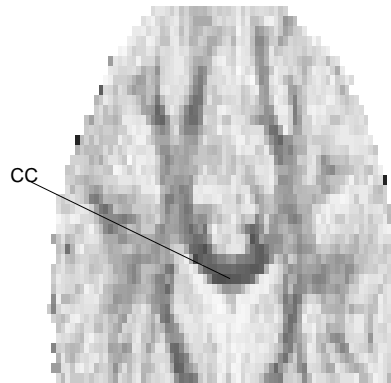
Figure B.4: Perturbation study of tractography algorithm performance in linear crossing software phantom as a function of intersection angle and Gaussian perturbation level. (a) 30 degree intersection (b) 60 degree intersection (c) 90 degree intersection
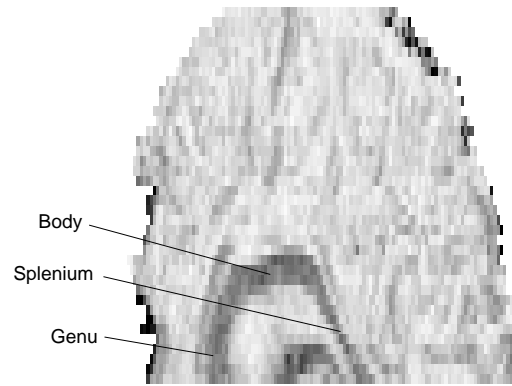
(a)

(b)

(c)

Figure B.5: Sample FA images used to determine seed points for corpus callosum estimates. Darker regions of FA maps have greater amounts of anisotropic diffusion, indicating presence of fiber bundles. Corpus callosum region denoted by abbreviation CC. (a) Sagittal view through left/right midline. Splenium, genu, and body regions of CC are labeled. (b) Axial view through body of CC. (c) Coronal view taken through splenium
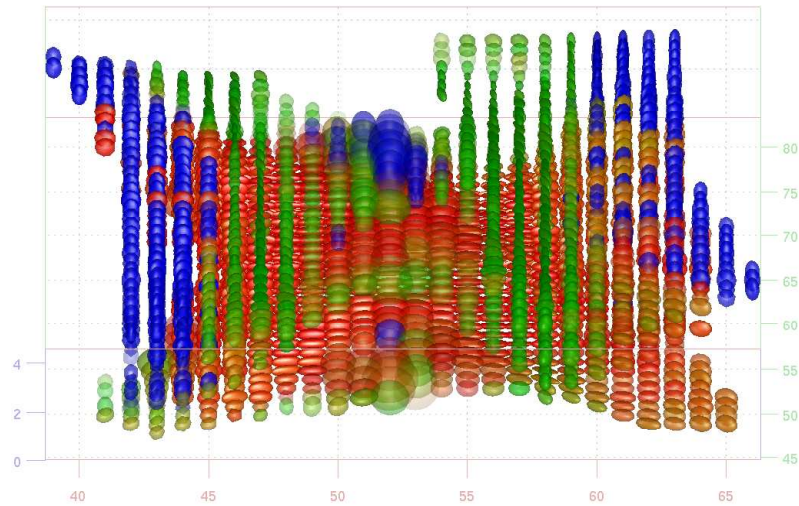
Figure B.6: Visualization of diffusion tensor ellipsoids in corpus callosum region of brain. Coloring of axis/ellipsoids reflects orientation of ellipsoidal structures. Transparency of ellipsoids reflects diffusion tensor anisotropy. A high degree of orientational coherence in the diffusion tensors within the corpus callosum is evident, with a large amount of red colored tensors running horizontally between the left and right regions of the brain within the body of the corpus callosum. Blue tensors toward outside of corpus callosum body describe tract orientations that move upward higher regions of the cerebrum. Green tensors are generally oriented above corpus callosum body and are not related to generally U shaped fiber tracts of corpus callosum
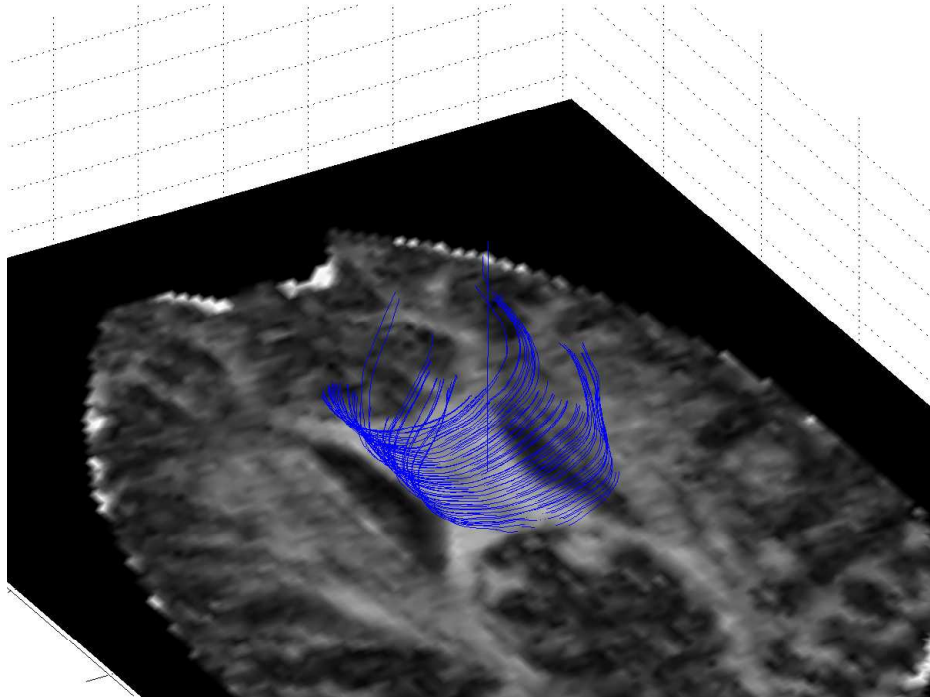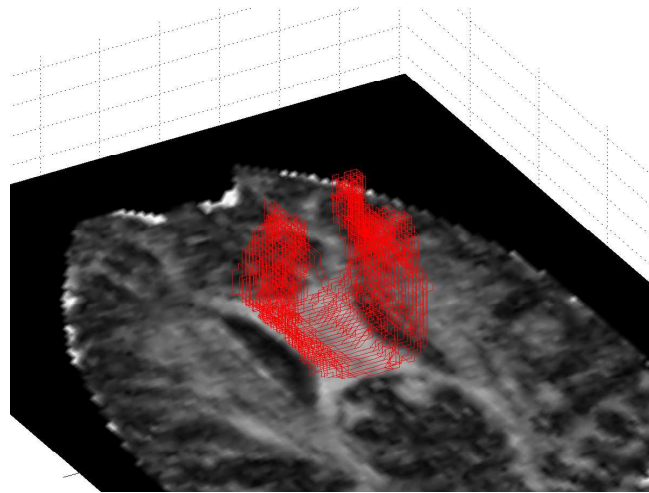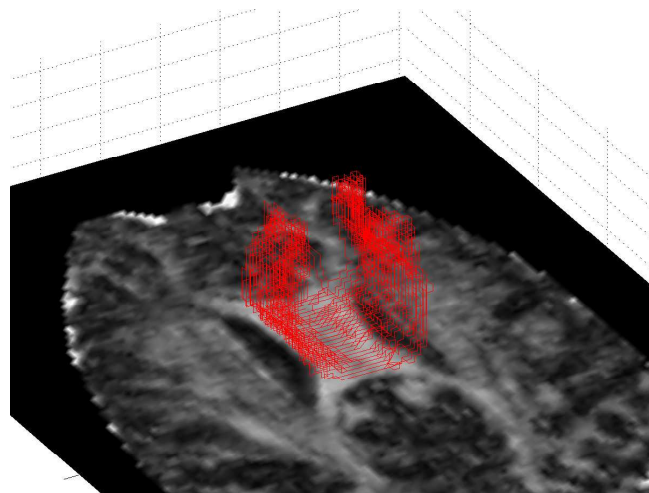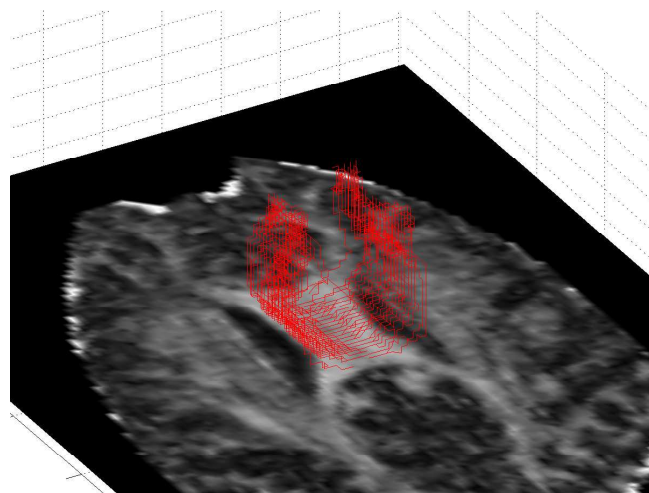
Figure B.7: Streamline tractography estimates in corpus callosum region of brain. Slice plane is FA image in plane used to seed streamline tracts

(a)

(b)

(c)

Figure B.8: Front propagation tractography results seeded in corpus callosum region of brain. Slice plane is FA image in plane used to seed FPT tracts (a) Highest 75% likelihood tracts (b) Highest 50% likelihood tracts (c) Highest 25% likelihood tracts
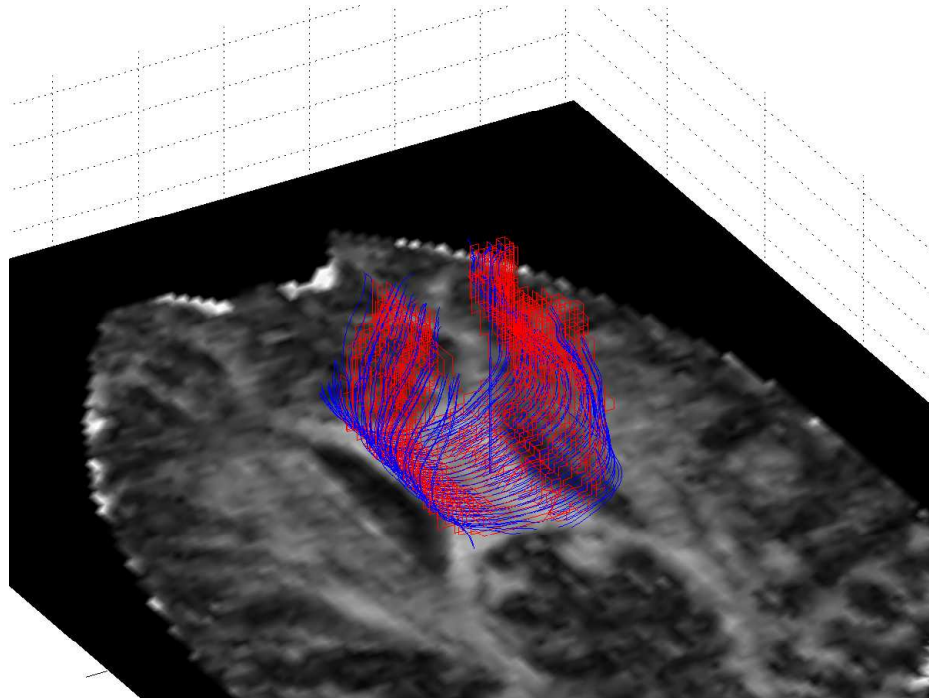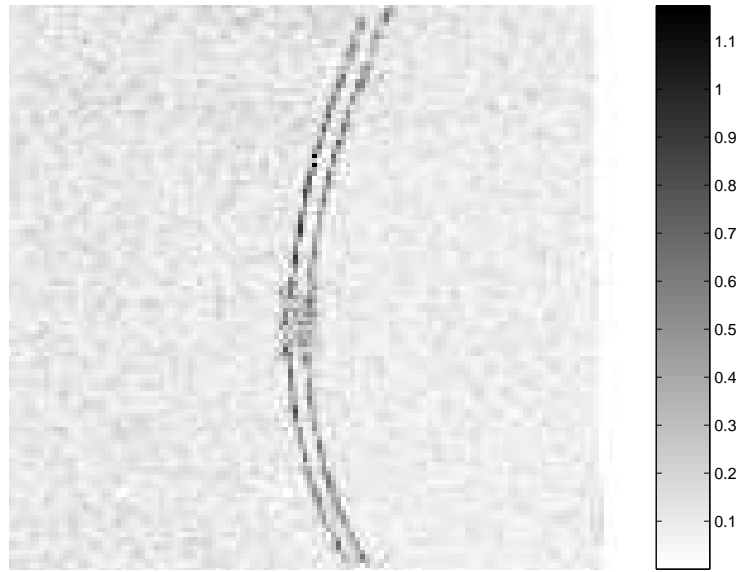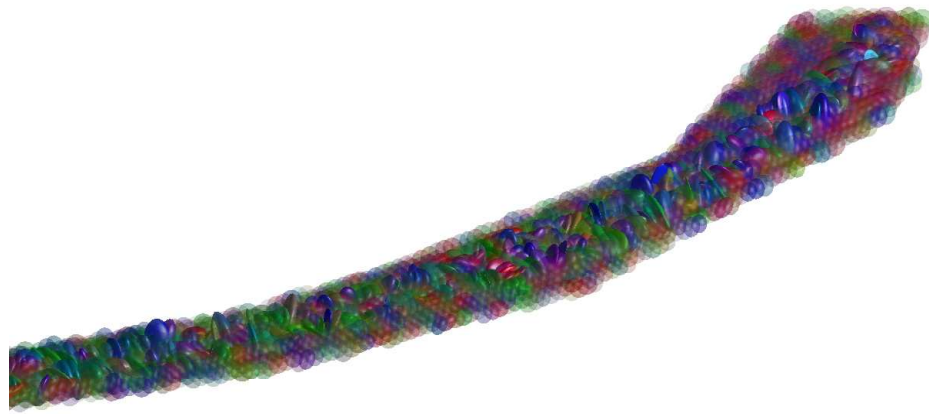
Figure B.9: Comparison of corpus callosum tract estimates of streamline and front propagation tractography algorithms. Streamline shown in blue, FPT shown in red. Streamline tracts appear smoother than FPT due to sub-voxel interpolation used to define streamline tracts. Both algorithms define same connectivity between corpus callosum and cerebrum.

(a)

(b)

Figure B.10: Results from attempted physical phantom. (a) FA image in which both crossing directions are visible, one in plane, one coming out of the image near the center of the in plane structure. FA metric indicates directionally dependent diffusion occurred within micro-capillary tubes. (b) Visualization of diffusion tensor ellipsoids in FA same plane as FA image of (a). Red, green, and blue colors reflect principal eigenvector orientations of tensors. Diffusion tensors oriented in direction of in plane tract should be red. Green and blue diffusion tensor orientations are generally orthogonal to tract direction. Orientational maximum of diffusion tensors in tissue phantom was extremely scattered and directionally inconsistent with actual tract orientation.

Bibliography

[1] Peter J. Basser and Sinisa Pajevic, "Statistical artifacts in diffusion tensor mri (dt-mri) caused by background noise," *Magnetic Resonance in Medicine*, vol. 44, pp. 41–50, 2000.

[2] Peter J. Basser, Sinisa Pajevic, Carlo Pierpaoli, Jeffrey Duda, and Akram Aldroubi, "In vivo fiber tractography using DT-MRI data," *Magnetic Resonance in Medicine*, vol. 44, pp. 625–632, 2000.

[3] Peter J. Basser, Sinisa Pajevic, Carlo Pierpaoli, Jeffrey Duda, and Akram Aldroubi, "Fiber tract following in the human brain using DT-MRI data," *IEICE Transactions on Information and Systems*, vol. E85-D, pp. 15–21, 2002.

[4] P.G. Batchelor, D. Atkinson, D.L.G. Hill, F. Calamante, and A. Connelly, "Anisotropic noise propagation in diffusion tensor MRI sampling schemes," *Magnetic Resonance in Medicine*, vol. 49, pp. 1143–1151, 2003.

[5] Howard C. Berg, *Random Walks in Biology*, Princeton University Press, Princeton, NJ, 1983.

[6] Kenneth A. Berman and Jerome Paul, *Fudamentals of Sequential and Parallel Algorithms*, Brooks Cole, Cincinnati, OH, 1980.

[7] A.I. Borisenko and I.E. Tarapov, *Vector and Tensor Analysis With Applications*, Dover Publications, Inc., New York, NY, 1979.

[8] Jennifer S. W. Campbell, Kaleem Siddiqi, and G. Bruce Pike, "White matter fibre tract likelihood evaluated using normalized rms diffusion distance," *Proceedings of the 10th International Society for Magnetic Resonance in Medicine annual meeting*, vol. 5, pp. 1130, 2002.

[9] Aziz M. Canny and Peter C.M. van Zijl, "Orientation-independent diffusion imaging without tensor diagonalization: Anisotropy definitions based on physical attributes of the diffusion ellipsoid," *Journal of Magnetic Resonance Imaging*, vol. 9, pp. 804–813, 1999.

[10] O. Ciccarelli, G.J.M Parker, C.A.M. Wheeler-Kingshott, G.J. Barker, P.A. Boulby, D.H. Miller, and A.J. Thompson, "From diffusion tractography to quantitative white matter tract measures: a reproducibility study," *NeuroImage*, vol. 18, pp. 348–359, 2003.

[11] Thomas E. Conturo, Nicolas F. Lori, Thomas S. Cull, Erbil Akbudak, Abraham Z. Snyder, Joshua S. Shimony, Robert C. McKinstry, Harold Burton, and Marcus E. Raichle, "Tracking neuronal fiber pathways in the living human brain," *Proc. Natl. Acad. Sci.*, vol. 96, pp. 10422–10427, 1999.

[12] Olivier Coulon, Daniel C. Alexander, and Simon R. Arridge, "A regularization scheme for diffusion tensor magnetic resonance images," in *Information Processing in Medical Imaging, IPMI 2001 (Davis, CA)*, M.F. Insana and R.M. Leahy, Eds., 2001, vol. 2082, pp. 92–105.

[13] Lin CP, Tseng WYI, Cheng HC, and Chen JH, "Validation of diffusion tensor magnetic resonance axonal fiber imaging with registered manganese-enhanced optic tracts," *NeuroImage*, vol. 14, pp. 1035–1047, 2001.

[14] Zhaohua Ding, John C. Gore, and Adam W. Anderson, "Classification and quantification of neuronal fiber pathways using diffusion tensor mri," *Magnetic Resonance in Medicine*, vol. 49, pp. 716–721, 2003.

[15] Kindlmann G, Weinstein D, and Hart D, "Strategies for direct volume rendering of diffusion tensor fields," *IEEE Transactions on visualization and computer graphics*, vol. 6, pp. 124–138, 2000.

[16] David Jensen, *The Human Nervous System*, Appleton-Century-Crofts, New York, NY, 1980.

[17] Derek K. Jones, Max Ervine, Martin Jeffree, and Joe Jarosz, "Cluster analysis of diffusion tensor magnetic resonance images in human head injury," *Neurosurgery*, vol. 47, pp. 306–314, 2000.

[18] Charles L. Lawson, *Solving Least Squares Problems*, Prentice-Hall, Inc., Englewood Cliffs, NJ, 1974.

[19] Mariana Lazar, David M. Weinstein, Jay S. Tsuruda, Khader M. Hasan, Konstantinos Arfanakis, M. Elizabeth Meyerand, Benham Badie, Howard A. Rowley, Victor Haughton, Aaron Field, and Andrew L. Alexander, "White matter tractography using diffusion tensor deflection," *Human Brain Mapping*, vol. 18, pp. 306–321, 2003.

[20] J.-F. Mangin, C. Poupon, C. Clark, D. Le Bihan, and I. Bloch, "Distortion correction and robust tensor estimation for mr diffusion imaging," *Medical Image Analysis*, vol. 6, pp. 191–198, 2003.

[21] Yoshitaka Masutani, Shigeki Aoki, Osamu Abe, Naoto Hayashi, and Kuni Otomo, "Mr diffusion tensor imaging: recent advance and new techniques for diffusion tensor visualization," *European Journal of Radiology*, vol. 46, pp. 53–66, 2003.

[22] Peter Nathan, *The Nervous System*, Oxford University Press, Oxford, UK, 1988.

[23] Margaret A. Niznikiewicz, Marek Kubicki, and Martha E. Shenton, "Recent structural and functional imaging findings in schizophrenia," *Current Opinion in Psychiatry*, vol. 16, pp. 123–147, 2003.

[24] Stanley Osher and Ronald Fedkiw, *Level Set Methods and Dynamic Implicit Surfaces*, Springer-Verlag, New York, NY, 2003.

[25] E. Ozarslan, B.C. Vemuri, and T.H. Mareci, "Fiber orientation mapping using generalized diffusion tensor imaging," in *ISBI 2004, From Nano to Micro (Arlington, Va)*, 2004.

[26] Athanasios Papoulis and S. Unnikrishna Pillai, *Probability, Random Variables and Stochastic Processes*, McGraw-Hill, New York, NY, 2002.

[27] Geoffrey J.M. Parker, Claudia A.M. Wheeler-Kingshott, and Gareth J. Barker, "Estimating distributed anatomical connectivity using fast marching methods and diffusion tensor imaging," *IEEE Transactions on Medical Imaging*, vol. 21, pp. 505–512, 2002.

[28] C. Poupon, C.A. Clark, V. Frouin, J Regis, I. Bloch, D. Le Bihan, and J.-F. Mangin, "Regularization of diffusion-based direction maps for the tracking of brain white matter fascicles," *NeuroImage*, vol. 12, pp. 184–195, 2000.

[29] William H. Press, Saul A. Teukolsky, William T. Vetterling, and Brian P. Flannery, *Numerical Recipes in C*, Cambridge University Press, New York, NY, 1988.

[30] J.A. Sethian, *Level Set Methods and Fast Marching Methods*, Cambridge University Press, Cambridge, UK, 1999.

[31] Warren D. Taylor, Edward Hsu, Ranga Rama Krishnan, and James R. MacFall, "Diffusion tensor imaging: Background, potential, and utility in psychiatric research," *Biological Psychiatry*, vol. 55, pp. 201–207, 2004.

[32] Kenshi Terajima and Tsutomu Nakada, "Ez-tracing: a new ready-to-use algorithm for magnetic resonance tractography," *Journal of Neuroscience Methods*, vol. 116, pp. 147–155, 2002.

[33] Gary A. Thibodeau and Kevin T. Patton, *Structure and Function of the Body*, Mosby-Year Book, Inc., St. Louis, MO, 1997.

[34] David Solomon Tuch, *Diffusion MRI of Complex Tissue Structure*, Ph.D. thesis, Massachusetts Institute of Technology, 2002.

[35] David S. Tuch, Timothy G. Reese, Mette R. Wiegell, Nikos Makris, John W. Belliveau, and Van J. Wedeen, "High angular resolution diffusion imaging reveals intravoxel white matter fiber heterogeneity," *Magnetic Resonance in Medicine*, vol. 48, pp. 577–582, 2002.

[36] Andrew Webb, *Introduction to Biomedical Imaging*, John Wiley and Sons, Inc., Hoboken, NJ, 2003.

[37] Van J. Wedeen, Timothy G. Reese, Vitaly J. Napadow, and Richard J. Gilbert, "Demonstration of primary and secondary muscle fiber architecture of the bovine tongue by diffusion tensor magnetic resonance imaging," *Biophysical Journal*, vol. 80, pp. 1024–1028, 2001.

[38] C.-F. Westin, S.E. Maier, H. Mamata, A. Nabavi, F.A. Jolesz, and R. Kikinis, "Processing and visualization for diffusion tensor mri," *Medical Image Analysis*, vol. 6, pp. 93–108, 2002.

[39] Dongrong Xu, Susumu Mori, Dinggang Shen, Peter C.M. van Zijl, and Christos Davatzikos, "Spatial normalization of diffusion tensor fields," *Magnetic Resonance in Medicine*, vol. 50, pp. 175–182, 2003.

[40] Song Zhang, Mark E. Bastin, David H. Laidlaw, Saurabh Sinha, Paul A. Armitage, and Thomas S. Deisboeck, "Visualization and analysis of white matter structural asymmetry in diffusion tensor MR imaging data," *Magnetic Resonance in Medicine*, vol. 51, pp. 140–147, 2004.

Vita
Alexander J. Taylor

Alexander Taylor was born in Jacksonville, Florida in January of 1980. Alexander lived in Woodbridge, Virginia from Age 1-18 and attended High School at Woodbridge Senior High. Alexander completed his BS degree in Electrical Engineering Summa Cum Laude at Virginia Polytechnic Institute and State University (Virginia Tech) in May, 2002. This document represents the partial completion of Alexander's MS degree in Electrical Engineering at Virginia Tech in May, 2004. Alexander's honours and awards include being awarded the Bradley Fellowship during his graduate studies and being an active member of the Golden Key National Honor Society. Alexander is a member of the Institute of Electrical and Electronics Engineers (IEEE).